Article

The biogeochemical balance of oceanic nickel cycling
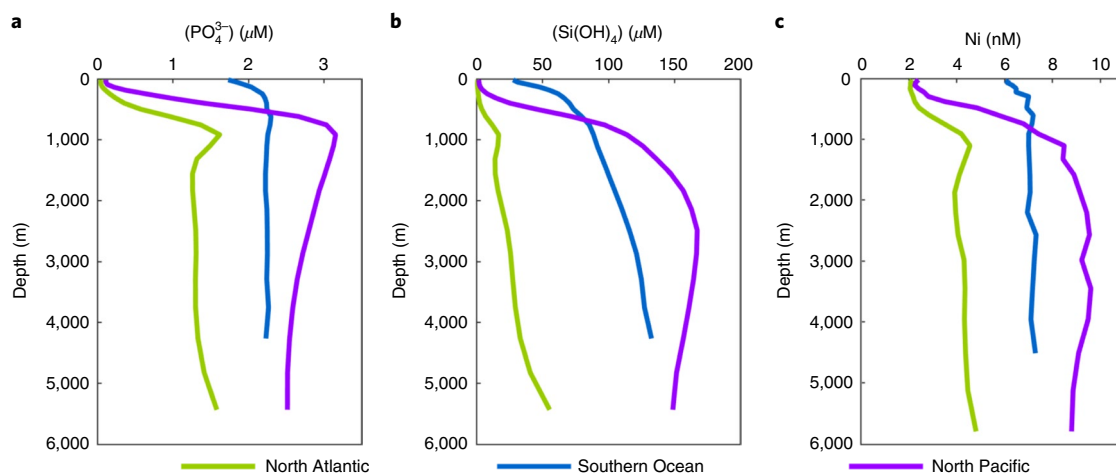
Seth G. John [1] ✉, Rachel L. Kelly[1], Xiaopeng Bian [1], Feixue Fu[2], M. Isabel Smith[1], Nathan T. Lanning [3], Hengdi Liang[1], Benoît Pasquier [1], Emily A. Seelen [1], Mark Holzer [4], Laura Wasylenki[5], Tim M. Conway [6], Jessica N. Fitzsimmons [3], David A. Hutchins [2] and Shun-Chung Yang [1]

Nickel is a biologically essential element for marine life, with the potential to influence diverse processes, including methanogenesis, nitrogen uptake and coral health, in both modern and past oceans. However, an incomplete view of oceanic Ni cycling has stymied understanding of how Ni may impact marine life in these modern and ancient oceans. Here we combine data-constrained global biogeochemical circulation modelling with culture experiments and find that Ni in oligotrophic gyres is both chemically and biologically labile and only minimally incorporated into diatom frustules. We then develop a framework for understanding oceanic Ni distributions, and in particular the two dominant features of the global marine Ni distribution: the deep concentration maximum and the residual pool of approximately 2 nM Ni in subtropical gyres. We suggest that slow depletion of Ni relative to macronutrients in upwelling regions can explain the residual Ni pool, and reversible scavenging or slower regeneration of Ni compared with macronutrients contributes to the distinct Ni vertical distribution. The strength of these controls may have varied in the past ocean, impacting Ni bioavailability and setting a fine balance between Ni feast and famine for phytoplankton, with implications for both ocean chemistry and climate state.

Nickel (Ni) is a biologically important metal, utilized in enzymes across all domains of life and important for diverse biogeochemical processes, including nitrogen fixation, nitrogen uptake, carbon fixation and methanogenesis[1,2]. Nickel concentrations in the modern ocean may be sufficiently limiting to influence important oceanic biological processes. In culture, for example, nitrogen fixation by cyanobacteria can be limited under certain conditions due to the Ni requirement of superoxide dismutase (SOD) and NiFe hydrogenase[3,4], phytoplankton nitrogen acquisition from urea can be limited by insufficient Ni for urease[5] and the growth of corals can be Ni limited due to inhibited urease activity of their symbionts[6]. However, Ni limitation of these processes in the oceans remains sparsely tested.

The availability of dissolved Ni to marine organisms is also thought to have played a crucial role in the evolution of life, due primarily to a Ni requirement for enzymes involved in methanogenesis. A Ni 'famine' in the oceans may have inhibited methanogenesis during the Archaean eon, allowing for the eventual rise of atmospheric oxygen[7], while Ni stable isotopes (δ^{60}Ni) suggest a small continued leak of Ni into the oceans from sulfide weathering, which supported enough methanogenesis to prevent a prolonged ice age during this time[8]. Similarly, δ^{60}Ni (δ^{60}Ni = ((^{60}Ni/^{58}Ni)sample/(^{60}Ni/^{58}Ni)standard 1)•1000) records from the Neoproterozoic Marinoan glaciation (~630 million years ago (Ma)) suggest that methanogenesis was crucial for termination of this glacial interval[9]. Fully understanding the controls on global marine Ni

[1]Department of Earth Sciences, University of Southern California, Los Angeles, CA, USA. [2]Department of Biological Sciences, University of Southern California, Los Angeles, CA, USA. [3]Department of Oceanography, Texas A&M University, College Station, TX, USA. [4]School of Mathematics and Statistics, University of New South Wales, Sydney, New South Wales, Australia. [5]Department of Chemistry and Biochemistry, Northern Arizona University, Flagstaff, AZ, USA. [6]College of Marine Science, University of South Florida, St Petersburg, FL, USA. ✉e-mail: sethjohn@usc.edu

Fig. 1 | The global marine distribution of Ni, P and Si. a–c, Dissolved water-column depth profiles of phosphate (PO_4^{3-}) (**a**), silicate ($Si(OH)_4$) (**b**) and Ni (**c**) all show nutrient-type distributions, although with different depth distribution and incomplete Ni depletion from the surface ocean. Macronutrient data are from the 2009 World Ocean Atlas, and Ni data are compiled here (Methods). Data are averaged for North Atlantic (20° N–30° N, 60° W–70° W), Southern Ocean (90° S–50° S, 120° W–160° E) and North Pacific (20° N–30° N, 140° W–150° W).

distribution in the modern ocean, therefore, provides insight into Ni's biological role in the past oceans and may provide predictive power for future ocean chemistry and climate state, where changes in global marine nutrient utilization patterns or ocean circulation could lead to Ni limitation of biota.

Nickel has a 'nutrient-type' distribution in the modern ocean, having higher concentrations in deep waters compared with the surface and increasing in concentration from the deep North Atlantic to the deep North Pacific. This pattern reflects the activity of the biological pump, which depletes nutrients from the surface ocean and accumulates them again within the deep ocean, increasing concentrations along the deep ocean 'conveyor belt' from the younger Atlantic to the older Pacific. This process is complicated by overprinting from circulation and mixing with surface waters having unique nutrient content, particularly the surface Southern Ocean, and vertical processes that transfer elements into the deeper ocean such as remineralization and scavenging[10–12].

However, despite a general nutrient-like distribution for Ni, and in stark contrast to most macronutrients and other micronutrient trace metals, a notable feature of the global ocean Ni distribution is a lack of complete Ni depletion in the surface ocean. Nickel is never depleted below ~1.7 nM, even in oligotrophic gyres where elements such as P, N, Si, Cd and Zn are drawn down to almost nothing (Fig. 1)[10]. Accordingly, a focus of study on the modern ocean Ni cycle has been to explain this disparity, with the current paradigm postulating that there is a ~2 nM pool of non-bioavailable Ni, attributed to either the slow kinetics of Ni reactivity in seawater[13] or the presence of ~2 nM strong Ni ligands in the surface ocean[14,15] that prevents biological uptake. Evidence for this point of view is mixed. For example, stable isotope ($\delta^{60}Ni$) signatures, which can be described by endmember mixing, have been used to infer an inert Ni pool that does not exchange with a bioavailable pool on the decadal timescales of upper-ocean mixing[16,17]. However, voltametric measurements of Ni speciation in seawater show only 10–50% of Ni is bound to strong organic ligands[2,18], complicating this interpretation.
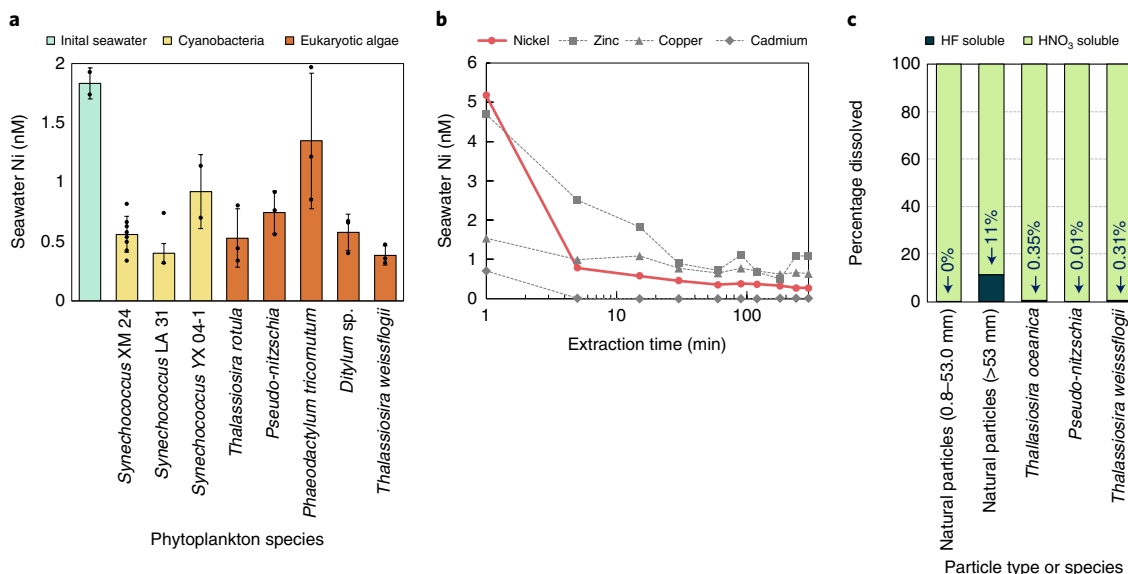
Nickel also displays a deep regeneration maximum, with a vertical distribution intermediate between that of the nutrients P and Si (Fig. 1). This feature has previously been attributed to a combination of faster uptake of Ni compared with N and P at high latitudes, similar to Si[19,20], and deeper regeneration of Ni compared with N and P due to the incorporation of Ni into diatom frustules[19,21]. The presumed incorporation of Ni into frustules is based on the co-location of Ni and Si at the outer edge of natural centric diatoms in synchrotron X-ray fluorescence images[19,21] and increased Ni uptake in natural diatom-rich communities under high silicate[19], which together suggest that ~50% of diatom cellular Ni could be present in frustules.

In this Article, we combine phytoplankton culturing, analysis of natural phytoplankton cells and global circulation biogeochemical modelling to challenge the existing paradigms. We show that the surface Ni pool is bioavailable and that the disparity between Ni and other nutrients is instead driven by slower depletion of Ni by biological uptake. Moreover, we show that the global distribution of dissolved Ni, including the deeper regeneration maximum, can be explained by a combination of uptake, regeneration, circulation and reversible scavenging.

Bioavailability of Ni in the surface ocean

We designed biological and chemical experiments to specifically test the lability of Ni in natural seawater. The bioavailability of Ni was tested by culturing phytoplankton in natural surface seawater from the oligotrophic North Pacific gyre amended with additional N, P and Si. Of the species studied, we found that all three isolates of the cyanobacterium *Synechococcus* and four of the five diatom species tested drew down Ni significantly below the initial 1.8 nM concentration (Fig. 2a). This demonstrates that the 1.8 nM Ni in natural surface seawater is indeed biologically available when additional macronutrients are provided to allow for continued phytoplankton growth. In addition, the chemical lability of the dissolved Ni in surface seawater was assessed by extracting metals out of waters taken from 350 m in the North Pacific onto resin beads functionalized with ethylenediaminetriacetate (EDTri-A) chelating groups at natural pH. We found that Ni was drawn down to ~0.5 nM within the first few minutes of the experiment (Fig. 2b), consistent with findings that surface-ocean Ni on a South Pacific transect crossing upwelling regions and the oligotrophic gyre was present primarily in labile forms[22]. These results show that most of the ~2 nM Ni in surface oligotrophic gyres is both chemically labile and bioavailable to biota, in contrast to earlier suggestions of an ~2 nM chemically inert Ni pool[14–17]. It is interesting to note, however, that both the chemical extractions and phytoplankton cultures reduced Ni below 2 nM but not below 0.3–0.5 nM, supportive of the possibility of ~0.3 nM of strong Ni binding ligands that could be chemically or biologically inert. Nevertheless, the majority of the 1.8 nM surface-ocean Ni (at least 80%) was chemically labile in our experiments and available for uptake.

Fig. 2 | Laboratory and field experiments test key features of Ni marine biogeochemistry. a, Seawater Ni bioavailaility. The bioavailability of Ni in natural waters was tested by using surface (20 m) seawater from the North Pacific subtropical gyre, with replete macronutrients and iron, to culture a variety of phytoplankton, and final seawater Ni concentrations were measured after cells entered stationary phase. **b**, Seawater Ni chemical lability. The chemical lability of Ni in natural seawater was tested by extracting Ni and other metals from subsurface (350 m) seawaters collected in the North Pacific subtropical gyre by resin beads with an EDTri-A functional group at natural pH. **c**, Nickel in diatom frustules. The presence of Ni within the silicate crystal lattice of diatom frustules was evaluated by dissolving diatom-rich particles in HNO_3 to extract soft-tissue Ni, then HF to access Ni contained within the silicate matrix; particles tested include natural marine particles in smaller (0.8 to 53 μm) and larger (>53 μm) size fractions and three species of laboratory cultured diatoms: *T. oceanica*, *Pseudo-nitzschia* and *T. weissflogii*.

If the surface dissolved Ni pool is bioavailable, an alternative mechanism is required to explain the disparity between Ni and other nutrients in the oligotrophic gyres. Instead of inert Ni, we hypothesize that Ni may be depleted more slowly than macronutrients from upwelling waters, such that ~2 nM is simply the amount of residual Ni 'left over' after phytoplankton production depletes the available macronutrients. This slower depletion of Ni from upwelling regions could thus account for the 2 nM Ni present in oligotrophic gyres, even if that Ni is bioavailable. We used a global biogeochemical circulation model to test this hypothesis. A range of Ni model simulations were constructed using the A Working Environment for Simulating Ocean Movement and Elemental cycling (AWESOME) within an ocean circulation inverse model (OCIM) framework[23], which allows biogeochemical processes to be embedded in the OCIM[24], a realistic global three-dimensional ocean circulation model (Methods). The OCIM representation as a steady-state matrix affords computational efficiency that allows for many biogeochemical process parameters to be optimized for the best fit to tracer observations[23]. For all model simulations, we parameterize Ni biological uptake as:

$$J_{UP} = \beta J_{UP-P} [Ni] \qquad (1)$$
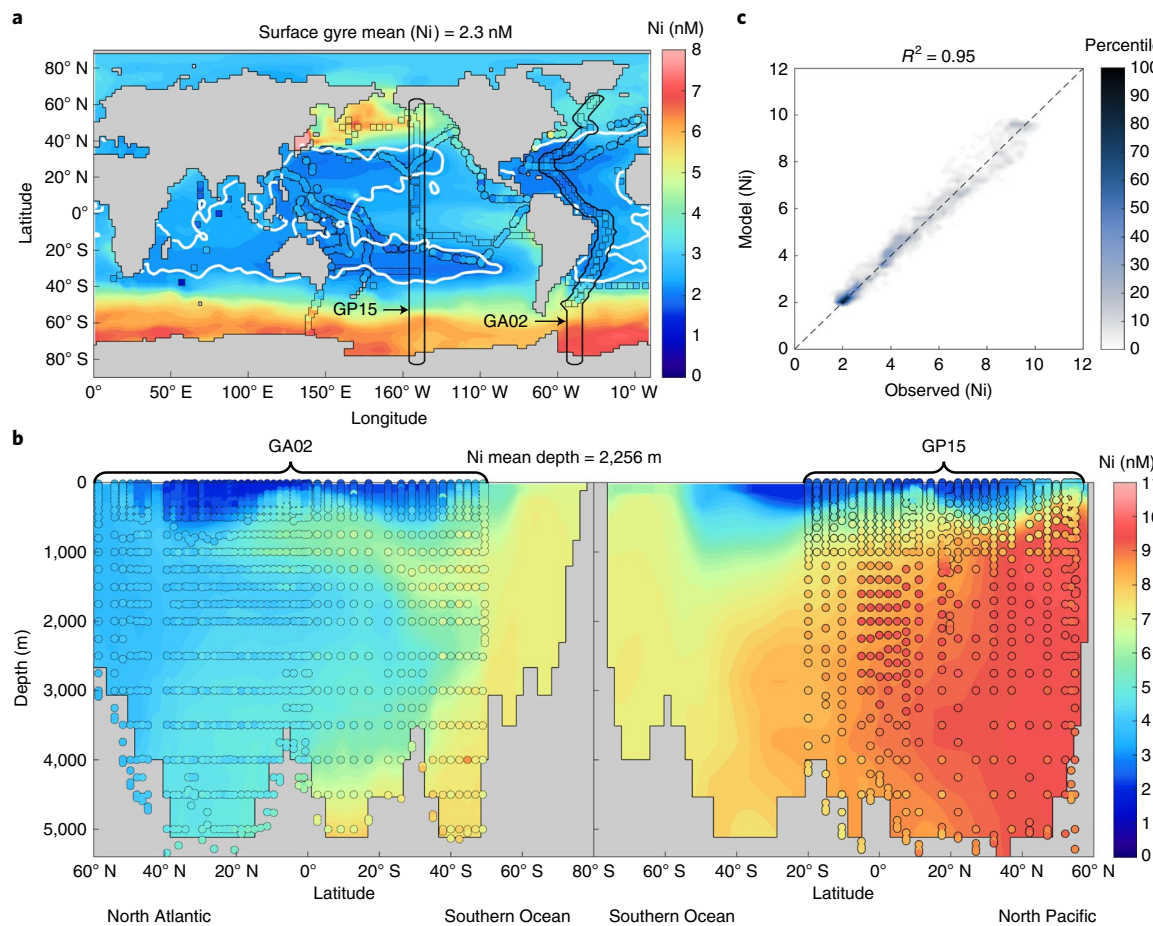
where J_{UP-P} is the P uptake rate diagnosed from a global OCIM model[12], and β is a globally uniform scaling factor that reflects the community average affinity of phytoplankton for Ni relative to P. Thus, Ni uptake is scaled to P uptake, where P uptake provides a proxy for net productivity in the surface oceans, and Ni uptake is linearly related to Ni concentrations on the basis of observations from culture studies[13,25]. This biologically assimilated Ni is assumed to be present in phytoplankton soft tissue and thus to remineralize at the same rate as P (following a power-law Martin curve profile with exponent $b = 0.92$). All models using this parameterization of biological uptake are able to reproduce the observation that Ni is not depleted in oligotrophic gyres (Fig. 3, Extended Data Figs. 1–7 and Supplementary Table 1; residual oligotrophic gyre Ni from 1.3 nM to 2.4 nM), consistent with our hypothesis that slower depletion of Ni compared with macronutrients can explain the ~2 nM Ni present in oligotrophic gyres.

The globally averaged value of phytoplankton Ni affinity (β) that we determine from model optimization may not apply in all real ocean regimes. Indeed, the β values measured for natural ocean phytoplankton vary by nearly 300-fold (Fig. 4b). However, the model-optimized β (0.14) is similar to that measured for natural Southern Ocean diatoms (0.23), which is expected because diatoms dominate productivity in upwelling regions such as the Southern Ocean, and nutrient uptake rates in the Southern Ocean are crucial for setting the residual Ni concentrations that remain in oligotrophic gyres (Fig. 4a). In short, once macronutrients are depleted from upwelling waters, little further Ni depletion can occur because net productivity is low. Nickel uptake is therefore macronutrient-limited, and productivity that does occur due to local mixing or upwelling will bring new Ni to the surface along with macronutrients. Differences in β in the modern oligotrophic gyres thus have little impact on Ni concentrations.

Fluxes of Ni into the deeper ocean

We similarly used modelling and experimentation to evaluate possible causes for the deeper Ni maximum compared with macronutrients N and P. As discussed, our modelling and experimentation do not support rapid uptake of Ni in upwelling waters and suggest instead that Ni is depleted more slowly than P. Further, a model that includes only biological uptake and regeneration of Ni in soft tissue fails to replicate key features of the global Ni distribution, instead yielding an overdepletion of Ni in the surface ocean and a distribution in the North Pacific with concentration maxima much shallower than observed (Extended Data Fig. 1). However, we do find that a model that allows for deeper regeneration of Ni due to incorporation of roughly 50% of diatom Ni into frustules is able to match observations, even in combination with slower depletion of Ni compared with macronutrients ($R^2 = 0.92$; Extended Data Fig. 2).

Fig. 3 | Model-predicted Ni distribution in the global oceans compared with observations for a model in which Ni is depleted more slowly than P from upwelling waters and remineralized more deeply than P. a, Comparison between observations (coloured circles) and optimized model output (background colour) for the surface ocean, with white lines delineating the boundaries of global oligotrophic gyres at 0.2 μM PO_4^{2-} and black lines showing the location of depth transects. **b**, A comparison between observations and optimized model output for depth transects, including GEOTRACES transects GA02 in the Atlantic and GP15 in the Pacific. The Ni mean depth reported above this panel refers to the average depth of model-predicted Ni in the global ocean (equation (14)), which can be compared with mean depths of 2,174 m and 2,533 m for P and Si, respectively, based on World Ocean Atlas 2009 data. **c**, The global fit between optimized model-predicted Ni and observations expressed as a percentage of maximum data density. Similar Ni distributions are produced by several models where Ni remineralizes with the same length scale as P and subject to reversible scavenging, making it difficult to distinguish between these processes (Extended Data Figs. 4–7).
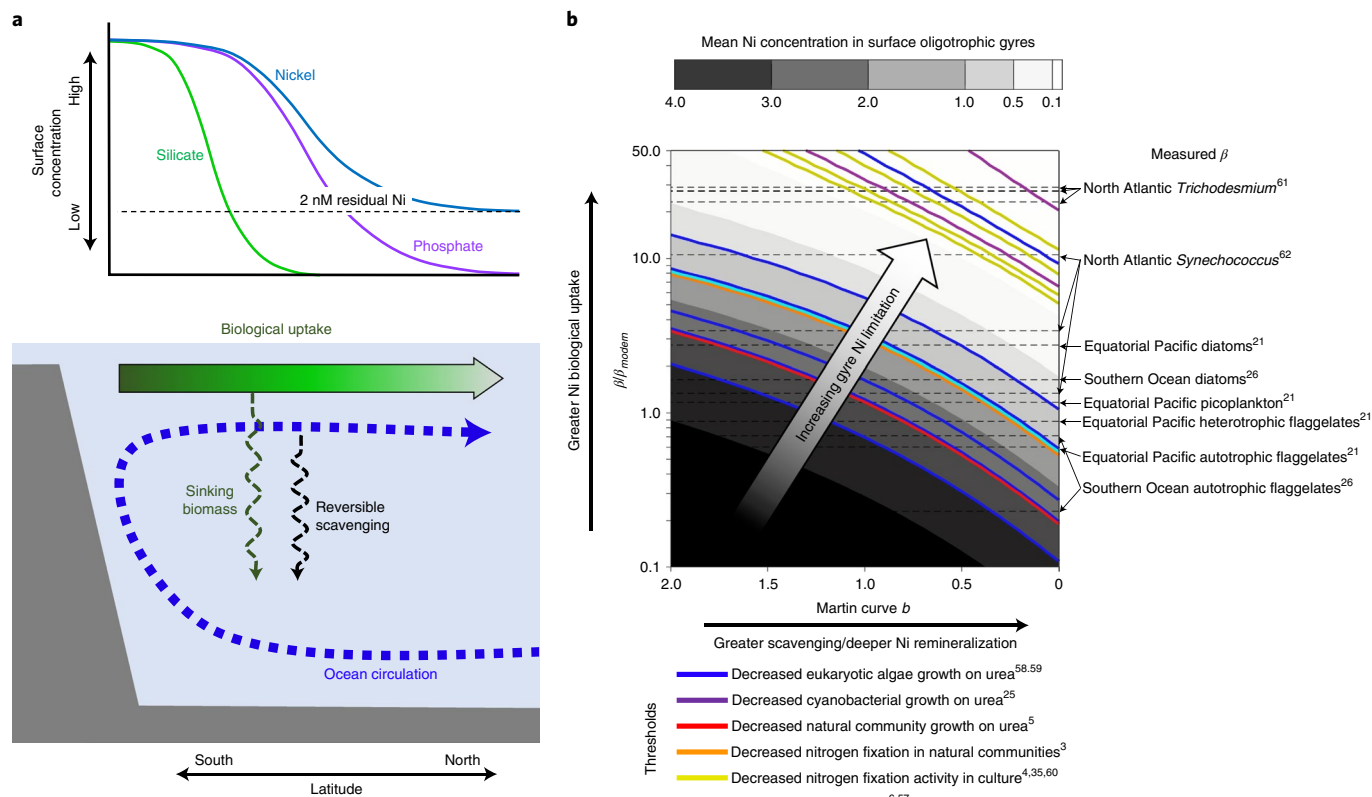
Critically, however, our analysis of both natural and cultured diatoms shows that very little Ni is incorporated into silicate diatom frustules (Fig. 2c). Within natural particles from the diatom-dominated eastern tropical North Pacific, more than 99.99% of the Ni in small particles (0.8–53 μm) was present in organic-matter phases dissolved in nitric acid (HNO_3), with just trace amounts of Ni present in the hydrofluoric acid (HF) soluble fraction that includes diatom silicate frustules. In a larger size class (>53 μm), 11% of the Ni was present in HF-soluble silicates, but even this portion seems more likely attributable to the presence of lithogenic silicate Ni rather than diatom frustules, considering the large size and the fact that these samples were collected near the continental margin, less than 50 km from the coastline. Analysis of diatoms cultured in the laboratory supports this conclusion, with <1% of Ni occurring in the frustules for *T. oceanica*, *Pseudo-nitzschia* and *T. weissflogii*. Studies of single-cell remineralization in the upper ocean also show Ni being quickly released from sinking diatom cells in the upper ocean, along with other soft-tissue elements[26].

Thus our modelling study and the shape of Ni concentration profiles both suggest that Ni is transferred to the deep ocean to a greater degree than the soft-tissue elements N and P. However, our analysis of diatoms shows the process responsible for transfer of Ni into the

deeper ocean is not incorporation into silicate frustules. Thus, we tested the ability of two different processes in the model to account for deep regeneration of Ni.

First, as with recent modelling studies of Zn[12] and in line with recent suggestions based on North Pacific data[27], we tested whether a model including reversible scavenging of Ni onto sinking particles could match observations. Various scavenging parameterizations were tested (Methods, Extended Data Figs. 3–8 and Supplementary Table 1), including scavenging onto particulate organic carbon (POC), scavenging following the patterns of Th and Pa scavenging, scavenging onto particulate Mn oxides and scavenging onto POC while allowing a power-law length scaling for the abundance of scavenging sites on POC, which is in line with observations that other elements such as Th exhibit an increased partitioning onto particles at greater depth[28]. Each of these models produced reasonable fits to observations (R^2 0.88 to 0.94), with the best fit achieved for the model including scavenging to POC with variable POC partitioning with depth (Fig. 3). The optimized partitioning between dissolved and particulate Ni (equation (7)) shows that with this model, just 1.4% of global ocean Ni is present in the scavenged (particulate) form at any moment. Still, the low scavenging rate acting over time can transfer large quantities of Ni into the abyssal ocean.

Fig. 4 | Key processes controlling global Ni cycling and their implications for past and future ocean Ni limitation. a, Nickel cycling in key upwelling regions, such as the Southern Ocean, is impacted by upwelling of nutrient-rich waters by ocean circulation and sinking of Ni and other nutrients back into the abyssal ocean within biomass and perhaps by reversible scavenging. As biological productivity depletes nutrients from upwelling waters, silicate is depleted most quickly due to its utilization in diatom frustules, followed by phosphate, with Ni being depleted even more slowly than phosphate, such that approximately 2 nM residual Ni is left over after macronutrients have been depleted. **b**, The impact of both biological Ni uptake affinity (β; Supplementary Table 2) and Ni sinking into the deep ocean (shown here as changes in the Martin curve exponent *b*) on surface-ocean oligotrophic gyre Ni concentrations is evaluated using the model. Changes in phytoplankton Ni uptake affinity compared with model-optimized values for the modern ocean (β/β_{modern}) and changes in Ni flux into the deep ocean by reversible scavenging and deep remineralization (reflected in *b*) both lead to changes in the amount of residual Ni present in oligotrophic gyres after macronutrient depletion (background colours). Changes to gyre Ni concentrations could impact past and future ocean life as the model-predicted concentrations span numerous thresholds at which various types of biological processes become limited (coloured lines). Phytoplankton Ni uptake affinities (β) measured in the field vary widely, as indicated by black dashed lines, indicating that large changes in β/β_{modern} could realistically arise from past and future changes in ocean biogeography.

Second, we tested whether slower remineralization of Ni compared with P, reflecting regional or species-specific variability in soft-tissue remineralization rates, could also match observations. While our initial model assumes a globally uniform Martin *b* exponent of 0.92, the attenuation of particulate-organic-matter flux with depth is known to vary regionally[29,30] and possibly by species, for example, due to mineral ballasting[31]. We therefore tested a model where Ni remineralizes with a Martin *b* exponent that is different from that for P. This model is optimized with *b* = 0.6, which corresponds to approximately a doubling in the transfer efficiency of particulate organic matter from 100 m to 1,000 m[30]. While this optimal *b* value for Ni is smaller than the optimal *b* for the model with a globally uniform *b* for P (0.92), and smaller than many estimates of *b* based on sediment-trap POC observations[32], it is similar to *b* from sediment-trap POC observed in the high-latitude North Pacific[29] and to model estimates of transfer efficiency at high latitudes[30]. A smaller *b* for Ni compared with P could therefore reflect that Ni is preferentially taken up by phytoplankton that grow in high-latitude upwelling regions, where higher Ni concentrations lead to higher phytoplankton Ni/P (equation (1)). This effect may be magnified if Ni is preferentially taken up by certain species that remineralize deeper in the water column. For example, diatoms in both the Southern Ocean and equatorial Pacific have higher Ni/P than other co-occurring species

(higher β; Fig. 4b), and diatom organic material could be exported to greater depth due to ballasting by silicate frustules or protection of organic cells from bacterial degradation, although Ni appears to be remineralized more quickly than P from individual diatoms[26], and global patterns of organic-matter remineralization indicate that diatoms do not transfer organic material to depth with greater efficiency than other organisms[31]. Because both the mechanisms of reversible scavenging and a deeper remineralization of Ni compared with P lead to models that match observations well, additional work is needed to determine which process or combination of processes dominates in the modern oceans. Future chemical, physical and biological analyses of Ni in sinking particles and experimental studies of Ni scavenging and remineralization in different locations and from different particle types will be helpful for definitively establishing the mechanism.

Implications for past and future ocean Ni limitation

Our model of Ni cycling in the modern ocean shows that the key biogeochemical controls on Ni distributions are (1) biological uptake and regeneration and (2) release of Ni deeper in the ocean than macronutrients, due to either reversible scavenging or deeper remineralization of biological Ni; both processes have probably changed in

magnitude in the geological past and may continue to shift in the future. Thus, we have examined how surface-ocean Ni concentration in oligotrophic gyres respond to changes in the Ni uptake affinity of phytoplankton (β) and regeneration depth (b), and compared the resulting gyre Ni concentrations to the concentration thresholds at which various marine biological processes become limited by Ni (Fig. 4b). The model-optimized value of β for the modern ocean is close to the measured uptake affinity for Southern Ocean diatoms ($\beta/\beta_{modern} = 1.6$), consistent with our view that Ni uptake in the Southern Ocean plays a key role in controlling Ni availability in modern ocean oligotrophic gyres. However, it is likely that Ni uptake affinity in important upwelling regions has varied through geological history as new life forms arose and grew to dominate ocean productivity. For example, before the origin of silicified diatoms 100–200 Ma, marine productivity was probably dominated by taxa including flagellated eukaryotes[33,34]. It is therefore notable that measured uptake affinities for autotrophic flagellates (Fig. 4b; $\beta/\beta_{modern} = 0.23–0.71$) are lower than for diatoms ($\beta/\beta_{modern} = 1.6–2.7$), suggesting a possible decrease in oligotrophic gyre Ni bioavailability with the origin of diatoms. Nitrogen-fixing diazotrophs have an especially high requirement for Ni, for use in hydrogenase and SOD enzymes[3,4,35], leading to higher Ni uptake affinities (Fig. 4b; for example, *Trichodesmium* $\beta/\beta_{modern} = 23–29$), which will deplete Ni from the surface ocean. This high Ni requirement also makes diazotrophs more susceptible to Ni limitation (Fig. 4b; for example, threshold isopleths for Ni limitation of N_2 fixation at 2 nM for natural communities and 0.04–67 pM in culture). Intervals of expanded ocean anoxia during Earth history have driven increased denitrification[36], which in turn requires higher N_2 fixation in the surface ocean, and even small increases in surface-ocean N_2 fixation could lead to rapid changes in Ni limitation as diazotrophs deplete Ni more quickly than other phytoplankton and are more easily limited by low Ni concentrations.

Changes in Ni release from sinking particles has the potential to change both the depth distribution of Ni and the total amount of Ni in the oceans. Over long timescales, burial of Ni by reaction with sedimentary Fe/Mn oxyhydroxides and Fe sulfides controls global ocean mean Ni concentrations[37]. Manganese oxyhydroxides, which are today the largest long-term sink for marine Ni[38], were essentially absent before the rise of oxygen at ~2.4 billion years ago (Ga) but increased in the Proterozoic Eon, then increased again with further oxygenation of the oceans at ~600 Ma (ref. [39]). Sulfides were uncommon before ~2.4 Ga, then most abundant during parts of the Proterozoic Eon and then less common since 600 Ma, except during several Palaeozoic and Mesozoic ocean anoxic events. To the extent that scavenging may control Ni distribution in the modern ocean, it has the potential for scavenging to deliver Ni to the sediments, where it can be sequestered on geological timescales. Similarly, changes in global-scale patterns in Ni uptake into different phytoplankton, which in turn may remineralize over different depth scales, will impact Ni sequestration in the deep ocean and eventually in the sediments. Such changes in Ni burial must have affected both surface-ocean processes, including nitrogen fixation and urea uptake, and processes that take place in the deeper ocean, including methanogenesis[7,8]. We therefore suggest that Ni bioavailability is uniquely susceptible to changes in ocean biogeochemistry, poised on a fine balance between feast and famine.

Online content

Any methods, additional references, Nature Research reporting summaries, source data, extended data, supplementary information, acknowledgements, peer review information; details of author contributions and competing interests; and statements of data and code availability are available at https://doi.org/10.1038/s41561-022-01045-7.

References

1. Alfano, M. & Cavazza, C. Structure, function, and biosynthesis of nickel-dependent enzymes. *Protein Sci.* **29**, 1071–1089 (2020).
2. Glass, J. B. & Dupont, C. L. in *The Biological Chemistry of Nickel* (eds Zamble, D., Rowinska-Zyrek, M. & Kozlowski, H.) 12–26 (The Royal Society of Chemistry, 2017); https://doi.org/10.1039/9781788010580-00012
3. Ho, T.-Y. Nickel limitation of nitrogen fixation in *Trichodesmium*. *Limnol. Oceanogr.* **58**, 112–120 (2013).
4. Tuo, S., Rodriguez, I. B. & Ho, T.-Y. H_2 accumulation and N_2 fixation variation by Ni limitation in *Cyanothece*. *Limnol. Oceanogr.* **65**, 377–386 (2020).
5. Dupont, C. L., Buck, K. N., Palenik, B. & Barbeau, K. Nickel utilization in phytoplankton assemblages from contrasting oceanic regimes. *Deep Sea Res. 1* **57**, 553–566 (2010).
6. Biscéré, T. et al. Enhancement of coral calcification via the interplay of nickel and urease. *Aquat. Toxicol.* **200**, 247–256 (2018).
7. Konhauser, K. O. et al. Oceanic nickel depletion and a methanogen famine before the Great Oxidation Event. *Nature* **458**, 750–753 (2009).
8. Wang, S.-J., Rudnick, R. L., Gaschnig, R. M., Wang, H. & Wasylenki, L. E. Methanogenesis sustained by sulfide weathering during the Great Oxidation Event. *Nat. Geosci.* **12**, 296–300 (2019).
9. Zhao, Z. et al. Active methanogenesis during the melting of Marinoan snowball Earth. *Nat. Commun.* **12**, 955 (2021).
10. Sunda, W. Feedback interactions between trace metal nutrients and phytoplankton in the ocean. *Front. Microbiol.* **3**, 204 (2012).
11. Sarmiento, J. L., Gruber, N., Brzezinski, M. A. & Dunne, J. P. High-latitude controls of thermocline nutrients and low latitude biological productivity. *Nature* **427**, 56–60 (2004).
12. Weber, T., John, S., Tagliabue, A. & DeVries, T. Biological uptake and reversible scavenging of zinc in the global ocean. *Science* **361**, 72–76 (2018).
13. Price, N. M. & Morel, F. M. M. Colimitation of phytoplankton growth by nickel and nitrogen. *Limnol. Oceanogr.* **36**, 1071–1077 (1991).
14. Mackey, D. J., O'Sullivan, J. E., Watson, R. J. & Dal Pont, G. Trace metals in the western Pacific: temporal and spatial variability in the concentrations of Cd, Cu, Mn and Ni. *Deep Sea Res. 1* **49**, 2241–2259 (2002).
15. Wen, L.-S., Jiann, K.-T. & Santschi, P. H. Physicochemical speciation of bioactive trace metals (Cd, Cu, Fe, Ni) in the oligotrophic South China Sea. *Mar. Chem.* **101**, 104–129 (2006).
16. Archer, C., Vance, D., Milne, A. & Lohan, M. C. The oceanic biogeochemistry of nickel and its isotopes: new data from the South Atlantic and the Southern Ocean biogeochemical divide. *Earth Planet. Sci. Lett.* **535**, 116118 (2020).
17. Lemaitre, N., Du, J., de Souza, G. F., Archer, C. & Vance, D. The essential bioactive role of nickel in the oceans: evidence from nickel isotopes. *Earth Planet. Sci. Lett.* **584**, 117513 (2022).
18. Achterberg, E. P. & Van Den Berg, C. M. G. Chemical speciation of chromium and nickel in the western Mediterranean. *Deep Sea Res. 2* **44**, 693–720 (1997).
19. Twining, B. S., Baines, S. B., Vogt, S. & Nelson, D. M. Role of diatoms in nickel biogeochemistry in the ocean. *Glob. Biogeochem. Cycles* **26** (2012).
20. Middag, R., de Baar, H. J. W., Bruland, K. W. & van Heuven, S. M. A. C. The distribution of nickel in the west-Atlantic Ocean, its relationship with phosphate and a comparison to cadmium and zinc. *Front. Mar. Sci.* **7**, 105 (2020).
21. Twining, B. S. et al. Metal quotas of plankton in the equatorial Pacific Ocean. *Deep Sea Res. 2* **58**, 325–341 (2011).
22. Saito, M. A., Moffett, J. W. & DiTullio, G. R. Cobalt and nickel in the Peru upwelling region: a major flux of labile cobalt utilized as a micronutrient. *Glob. Biogeochem. Cycles* **18** (2004).
23. John, S. G. et al. AWESOME OCIM: a simple, flexible, and powerful tool for modeling elemental cycling in the oceans. *Chem. Geol.* **533**, 119403 (2020).

24. DeVries, T., Holzer, M. & Primeau, F. Recent increase in oceanic carbon uptake driven by weaker upper-ocean overturning. *Nature* **542**, 215 (2017).
25. Dupont, C. L., Barbeau, K. & Palenik, B. Ni uptake and limitation in marine *Synechococcus* strains. *Appl. Environ. Microbiol.* **74**, 23–31 (2008).
26. Twining, B. S. et al. Differential remineralization of major and trace elements in sinking diatoms. *Limnol. Oceanogr.* **59**, 689–704 (2014).
27. Zheng, L., Minami, T., Takano, S., Ho, T.-Y. & Sohrin, Y. Sectional distribution patterns of Cd, Ni, Zn, and Cu in the North Pacific Ocean: relationships to nutrients and importance of scavenging. *Glob. Biogeochem. Cycles* **35**, e2020GB006558 (2021).
28. Le Gland, G., Aumont, O. & Mémery, L. An estimate of thorium 234 partition coefficients through global inverse modeling. *J. Geophys. Res. Ocean.* **124**, 3575–3606 (2019).
29. Buesseler, K. O. et al. Revisiting carbon flux through the ocean's twilight zone. *Science* **316**, 567–570 (2007).
30. Weber, T., Cram, J. A., Leung, S. W., DeVries, T. & Deutsch, C. Deep ocean nutrients imply large latitudinal variation in particle transfer efficiency. *Proc. Natl Acad. Sci. USA* **113**, 8606 LP–8608611 (2016).
31. Klaas, C. & Archer, D. E. Association of sinking organic matter with various types of mineral ballast in the deep sea: implications for the rain ratio. *Glob. Biogeochem. Cycles* **16**, 14–63 (2002).
32. Berelson, W. M. The flux of particulate organic carbon into the ocean interior: a comparison of four US JGOFS regional studies. *Oceanography* **14**, 59–67 (2001).
33. Kooistra, W. H. C. F., Gersonde, R., Medlin, L. K. & Mann, D. G. in *Evolution of Primary Produces in the Sea* (eds Falkowski, P. G. & Knoll, A. H.) 207–249 (Academic Press, 2007); https://doi.org/10.1016/B978-012370518-1/50012-6
34. Medlin, L. K., Kooistra, W. C. H. F. & Schmid, A.-M. M. in *The Origin and Early Evolution of the Diatoms: Fossil, Molecular and Biogeographical Approaches* (eds Witkowski, A. & Siemińska, J.) 13–35 (Polish Academy of Sciences, 2000).
35. Rodriguez, I. B. & Ho, T.-Y. Diel nitrogen fixation pattern of *Trichodesmium*: the interactive control of light and Ni. *Sci. Rep.* **4**, 4445 (2014).
36. Algeo, T. J., Meyers, P. A., Robinson, R. S., Rowe, H. & Jiang, G. Q. Icehouse–greenhouse variations in marine denitrification. *Biogeosciences* **11**, 1273–1295 (2014).
37. Little, S. H. et al. Towards balancing the oceanic Ni budget. *Earth Planet. Sci. Lett.* **547**, 116461 (2020).
38. Ciscato, E. R., Bontognali, T. R. R. & Vance, D. Nickel and its isotopes in organic-rich sediments: implications for oceanic budgets and a potential record of ancient seawater. *Earth Planet. Sci. Lett.* **494**, 239–250 (2018).
39. Roy, S. Sedimentary manganese metallogenesis in response to the evolution of the Earth system. *Earth Sci. Rev.* **77**, 273–305 (2006).

Methods

Chemical lability of Ni

The chemical lability of Ni and other metals in natural subsurface seawater (350 m) was tested on seawater collected in the oligotrophic North Pacific Subtropical Gyre. Seawater was cleanly collected aboard the RV *Kilo Moana* on the MESO-SCOPE cruise in early July 2017 using a trace metal clean rosette and Niskin bottles at Station ALOHA (22.75° N, 158° W), filtered using a 0.2 μm AcroPak capsule filter with a Supor membrane and immediately frozen after collection to preserve organic speciation.

The concentration of inert Ni was determined by extracting labile metals onto a Nobias PA-1 resin with EDTri-A functional groups (Hitachi). The method was based on similar earlier work that evaluated Ni and Cu lability by extraction of labile metals onto Chelex resin with iminodiacetate resins; this method was found to provide similar results to traditional methods using a dimethylglyoxime competitive ligand[40]. In the laboratory, the seawater sample was thawed, and 1 ml Nobias resin was added to 250 ml seawater without pH adjustment. Aliquots of 15 ml were removed over the course of the next 3 h and filtered using a polyethylene syringe with a 0.2 μM Supor polyethersulfone filter to ensure that resin was completely removed. Sample aliquots were then acidified for 5 d with 0.1% perfluoroalkoxy- (PFA-) distilled HCl before analysis. Seawater metal concentrations were analysed at the University of Southern California. Briefly, samples were amended with a multi-element isotope spike, concentrated into 5% HNO_3 using a SeaFast and analysed on an Element 2 inductively coupled plasma mass spectrometer (Thermo) using isotope dilution. A complete description of seawater processing and analytical protocols is provided in ref. [41].

All bottles and tubes used for this experiment and other experiments described in the following were rinsed with ultrapure water (18.2 MΩ), soaked overnight in a 5% citranox solution, rinsed again with ultrapure water, soaked in 10% hydrochloric acid for one week and rinsed again with ultrapure water.

Biological availability of Ni

The bioavailability of Ni in surface-ocean oligotrophic gyre seawater was tested using the seawater collected at 20 m from the same cruise described in the preceding. As for the chemical lability experiments, seawater was preserved by freezing after collection to best maintain the natural ligand binding capacity for Ni. Two major taxonomic groups of phytoplankton, diatoms and cyanobacteria, were used in the experiments. For diatom growth, the seawater was amended with 80 μM NO_3^-, 5 μM PO_4^{3-}, 100 μM SiO_4^{2-} and 20 nM Fe; for *Synechococcus*, the same nutrients were added except that silica was omitted. No vitamins and other trace metals were added to the seawater media.

Three isolates of *Synechococcus* (coastal strains XM 24, LA 31 and YX 04-1 from the open oligotrophic South China Sea) and five species of coastal diatoms (*Thalassiosira weissflogii* and *Pseudo-nitzschia* sp. isolated from the Southern California Bight, USA, *Ditylum* sp. and *Thalassiosira rotula* isolated from Narragansett Bay, Rhode Island, USA, and *Phaeodactylum tricornutum* CCMP 632 isolated from Blackpool, England, UK) were grown for this study. All were cultured at a light intensity of 150 uE m^{-2} s^{-1} under a 12/12 light/dark cycle in triplicate 25 ml polycarbonate bottles. Diatoms were grown at 19 °C, *Synechococcus* YX 04-1 was grown at 30 °C, *Synechococcus* LA 31 was grown at 27 °C and *Synechococcus* XM 24 was grown in three experiments at 27 °C, 32 °C and 36 °C to assess whether growth rate had an impact on Ni accumulation. Because the results for *Synechococcus* XM 24 at all three temperatures were similar, the experimental results are plotted together. In vivo fluorescence was measured daily on a fluorometer to monitor phytoplankton growth. Once late exponential growth phase was reached, additional macronutrients and iron were added to promote further growth. Culture samples were syringe filtered through 25 mm, 0.2 μm Supor filters to collect filtrate for nutrient and trace metal analyses. The filtered water samples were frozen in 15 ml trace metal clean centrifuge tubes at −20 °C then acidified for several weeks with 0.1% HCl and analysed as described in the preceding. Because many of these isolates are coastal strains with potentially less efficient Ni uptake systems than open-ocean strains, the extent of uptake should probably be taken as minimum estimates of Ni bioavailability in the gyre water tested, and it is possible that open-ocean strains are capable of depleting Ni below the ~ 0.5 nM level observed in our experiments.

Ni concentrations in biogenic silicate

Nickel concentrations in diatom soft tissue and diatom biogenic silicate were determined for three species of diatoms grown in laboratory culture and two natural particle assemblages collected from diatom-rich waters of the eastern tropical North Pacific. For both sample types, samples were first treated with HNO_3 to digest organic soft-tissue Ni, then with HF to dissolve silicate frustules, using procedures based closely on previous work that has demonstrated that a hot HNO_3 treatment does not dissolve diatom frustule silicate[42-44]. The presence of diatom frustules following HNO_3 digestion was visually confirmed by the presence of a white material that settled quickly during rinsing (presumably diatom frustules). The fidelity of the method was additionally confirmed for the natural samples by microscopy, which showed abundant and well-preserved centric and pennate diatom frustules free of organic material (as well as siliceous shells of a few silicoflagellates and radiolarians) following the HNO_3 treatments (Extended Data Fig. 9).

Cultured diatoms included two centric species (*T. oceanica* and *T. weissflogii*) and a pennate species (*Pseudo-nitzschia*). Diatoms were cultured in 500 ml modified Aquil medium[45] containing 25 μM EDTA, 250 nM total Fe and 5 μM total Ni. Diatoms were collected at the end of the exponential growth by centrifugation at 3,220 RCF in 50 ml clean low-density polyethylene tubes. After centrifuging, most of the supernatants were decanted, and diatoms from all ten tubes were pipetted into a new 50 ml tube. This tube was centrifuged again, and the supernatant was pipetted out. The diatoms were then cleansed by an oxalate–EDTA reagent (10 ml) to remove surface-bound metals[46] and 20 ml surface oligotrophic seawater from North Pacific to remove any residual oxalate–EDTA solution and culture medium.

The washed diatom samples were then transferred into 7 ml PFA vials for sample digestion. Organic matter (diatom soft tissue) was digested first by adding 5 ml 8 M HNO_3 and reacting for 2 d on a hot plate at 120 °C. Samples were then uncapped and heated overnight to dryness at 120 °C. These dried samples were redissolved by adding 5 ml 0.1 M HNO_3, containing 10 ppb In, and transferred into acid-washed 15 ml low-density polyethylene centrifuge tubes. The tubes were then centrifuged at 3,220 RCF for 5 min to separate the undissolved frustules. Supernatant containing dissolved soft-tissue elements was pipetted into clean 15 ml tubes for Ni concentration measurement. The frustule portion was rinsed three times with 10 ml Milli-Q, followed by centrifugation and removal of the rinse by pipette. Frustules were then resuspended into 1 ml 28 M HF and transferred into a clean 7 ml PFA vial. The capped vials were heated at 120 °C for 1 h to completely dissolve the frustules and heated to dryness after that. The residue was then redissolved by 5 ml 0.1 M HNO_3, containing 10 ppb In, transferred to clean 15 ml tubes and analysed along with the soft-tissue digest by In standard addition on an Element 2 inductively coupled plasma mass spectrometer.

A similar procedure was used to test for the incorporation of Ni into the biogenic silica of natural diatoms. Natural marine particles were collected in the eastern tropical North Pacific upwelling region off Mexico (20.4° N, 106.2° W) in April 2018 aboard the RV *Roger Revelle*. Phytoplankton communities in this area are typically dominated by diatoms[47], which was corroborated by microscopic examination of these samples (Extended Data Fig. 8). Particles were concentrated from seawater using a McLane pump (McLane Research Laboratories) equipped with a 4 mm mesh screen, a 53 μm Sefar polyester mesh prefilter and a 0.8 μm Pall Supor polyethersulfone filter, using recommended methods in the GEOTRACES sample and sample-handling protocols[48].

The samples were collected at subsurface depths of 190 m (large size-fraction particles; >53 μm) and 280 m (small size-fraction particles; 0.8–53 μm), and thus some of the organic material that was originally present in the diatoms at the surface may have been remineralized, leaving behind a higher proportion of diatom frustules. In addition, the location of samples close to the continental margin raises the possibility that some of the Ni present in the HF-soluble fraction may be due to the presence of lithogenic material. The samples we analysed were specifically chosen because they visibly contained the greatest amount of insoluble white matter, assumed to be composed primarily of diatom frustules, yet we cannot rule out the presence of lithogenics. For both of these reasons, the reported HF-soluble Ni in these samples should be considered a maximum amount that would be present in natural diatom frustules, with a possible additional contribution from non-diatom lithogenic Ni.

The organic fraction of each sample was digested by placing sample filters in a 25 ml acid-washed PFA vial containing 5 ml 8 M HNO$_3$. Samples were digested in capped vials on a hot plate at 120 °C for 12 h. After digestion, the filters were removed, placed into acid-washed 15 ml centrifuge tubes and rinsed with 5 ml Milli-Q water. The Milli-Q water was transferred back into the digestion vials. The digest solution was then heated on a hot plate at 80 °C to dryness, then resuspended by adding 10 ml 4 M HNO$_3$. This solution was transferred into acid-washed 15 ml centrifuge tubes and centrifuged at 805 RCF for 5 min to segregate insoluble particles and filter debris. The supernatant of each sample was pipetted into an acid-washed 15 ml centrifuge tube. Any residual dissolved organic matter was removed by five sequential rinses, in which 10 ml Milli-Q water was added, particles were resuspended by hand shaking, particles were re-separated by centrifugation at 805 RCF for 5 min and the supernatant was discarded. After rinsing, 1 ml 28 M HF and 2 ml 14 M HNO$_3$ were added to each tube, and particles were resuspended by hand shaking then poured with the acids into a 7 ml acid-washed PFA vial. The samples were fully dissolved in capped vials on a hot plate at 120 °C for 1 h. Finally, the solution was heated at 80 °C to dryness and then redissolved by adding 5 ml 4 M HNO$_3$. A small portion of HNO$_3$- or HF + HNO$_3$digested samples was taken into acid-washed 15 ml centrifuge tubes, diluted by ten times and amended with In standard solution with a matrix of 0.1 M nitric acid to reach a final concentration of 1 ppb In. The diluted samples were analysed for Ni concentrations as described in the preceding for cultured biogenic silicate.

Global Ni datasets

A global Ni observation dataset was compiled to test Ni biogeochemical models. The majority of global data were composed of all Ni concentration measurements reported in the GEOTRACES 2017 International Data Product[49]. Surface-ocean Ni concentration data from the *Tara* Pacific expedition was also included, with sampling and analytical methods described in ref. [50]. Data were also added for samples collected during the US GEOTRACES GP15 transect, which was completed in September to October 2018 and followed a transect near 152° W from 56° N to 20° S, sailing from near Alaska to near Tahiti. For this cruise, dissolved Ni concentrations were measured in aliquots of the same Go-Flo bottle sample both at the University of Southern California (according to the methods described for the chemical and biological lability experiments) and at Texas A&M University. Ni concentration analyses at Texas A&M University followed similar SeaFAST pico analytical methods as at the University of Southern California following previously published methods[51]. Agreement between the datasets was excellent, with a slope of 0.997 and an R^2 of 0.999. Therefore, the combined dataset was produced by averaging together the Ni concentration measurements from both labs, except in cases where only one lab measured samples or only one lab reported a clearly anomalous result (<5% of samples).

Global Ni biogeochemical model

Nickel global biogeochemical modelling was performed using the AWESOME OCIM modelling environment[23]. Seven models were tested for this work (Extended Data Figs. 1–7), and model parameters were optimized by minimizing the volume-weighted squared misfit between model tracer concentration and the compiled Ni observations (using MATLAB's fminsearch). The global ocean mean Ni concentration, Ni$_{mean}$, was optimized for each model. All models used the same parameterization of biological uptake, where Ni uptake is proportional to net productivity (equation (1)), as inferred from net P uptake and local Ni concentrations, based on culture data showing that cellular Ni/P is nearly linearly related to ambient dissolved Ni concentration[13,25]. Model performance with additional processes was tested as follows: (1) no additional processes, (2) uptake of Ni into diatom frustules, (3) reversible scavenging onto POC, (4) reversible scavenging in the pattern of Th, (5) reversible scavenging in the pattern of Pa, (6) reversible scavenging onto particulate Mn oxides and (7) reversible scavenging onto POC where the depth distribution of POC scavenging sites is slightly different from the distribution of POC. Model-optimized parameters and performance assessment metrics are presented in Supplementary Table 1.

Our models do not include external sources or sinks, such that they behave as 'closed systems', where particulate Ni that reaches the seafloor is immediately redissolved. We constrained the total inventory of Ni by restoring Ni concentrations to Ni$_{mean}$ everywhere with a 1 Myr timescale (implemented via AWESOME OCIM's conc function). Because the model does not include external sources and sinks, and because the OCIM circulation is optimized for large ocean basins, our model is expected to accurately reproduce global-scale patterns of tracer distribution but to fare less well in confined regional settings where external sources could be more important, such as the Mediterranean, the Sea of Japan and the Arctic Ocean.

The general continuity equation describing the steady-state distribution of Ni in the oceans for all models is:

$$\frac{dNi}{dt} = T\,Ni - J_{UP} + J_{REM} + J_{SCAV} \tag{2}$$

where T is the OCIM transport matrix from ref. [52], J_{UP} is the surface-ocean biological uptake of Ni as described in the main text (equation (1)), J_{REM} is the remineralization of Ni from sinking soft-tissue organic matter and J_{SCAV} reflects the downward transport of Ni due to reversible scavenging, where applicable.

Biological uptake of Ni into soft tissue is described in equation (1). The particle flux for remineralization of this soft-tissue Ni is:

$$F_z = F_0 \left(\frac{z}{z_0}\right)^{-b} \tag{3}$$

where F_z is the flux at depth z, F_0 is the flux at the base of the model euphotic zone, z is depth, z_0 is the depth of the base of the euphotic zone and b is the 'Martin curve' scaling parameter from the P model of ref. [12], which has a value of 0.92. The remineralization of soft-tissue Ni can therefore be described by the flux divergence:

$$J_{REM} = -\frac{\partial F_z}{\partial z} \tag{4}$$

For the model in which Ni is incorporated into diatom frustules, Ni incorporation ($J_{UP\,frustules}$) is parameterized in the same general fashion as for the uptake of Ni into soft tissue described in equation (1), by:

$$J_{UP\,frustules} = \beta_{Si} J_{UP-Si} [Ni] \tag{5}$$

where $J_{UP\text{-}Si}$ is the Si uptake rate diagnosed from a global OCIM model of Si cycling by Holzer et al.[53] updated to use the more recent OCIM

circulation of Devries et al.[52], and β_{Si} is a scaling factor that reflects the affinity of phytoplankton for Ni compared with Si. Nickel is assumed to be released from dissolving frustules at the same rate as silicate redissolution in the Holzer et al. model[53].

The downward transport of Ni due to reversible scavenging is represented by calculating the amount of scavenged Ni as a function of a partition constant (K) and the concentration of particle sites available for scavenging (S):

$$[Ni_{scav}] = K S [Ni] \tag{6}$$

and assigning a sinking rate for particles, for which we typically use 100 m d^{-1}. Once model runs have been optimized, this same equation allows us to calculate the relative fraction of Ni present in the particulate phase (Ni_{scav}) compared with the dissolved phase (Ni). The downward transport of Ni due to reversible scavenging can then be calculated using an 'effective sinking rate' (ESR) for Ni given by:

$$ESR = \frac{Ni_{SCAV}}{Ni} w \tag{7}$$

where ω is the particle sinking rate, and calculating the scavenging flux at each depth by:

$$J_{SCAV} = \frac{\partial}{\partial z} (-ESR\,[Ni]) \tag{8}$$

Reversible scavenging of Ni onto POC was implemented using the AWESOME OCIM revscavPOC function, where the global distribution of POC in the surface ocean was based on satellite observations, and the vertical attenuation of POC flux was based on a Martin curve power-law distribution with a b value of 0.92. The downward flux of Ni due to reversible scavenging onto POC can thus be summarized by combining equations (7–9) to yield:

$$J_{scav} = K w \frac{\partial}{\partial z} ([POC]\,[Ni]) \tag{9}$$

Reversible scavenging in the patterns of Th and Pa was based on the scavenging dynamics in a biogeochemical circulation model of ^{230}Th and ^{231}Pa by van Hulten et al.[54]. This model allows for ^{230}Th and ^{231}Pa scavenging onto POC, calcium carbonate and biogenic silica, each of which occurs in two different size classes. With two size classes of particles, the faster-sinking particles will be much more effective at transferring elements to the deep ocean, and we therefore combine the total effect of scavenging onto all particle types and size classes into an ESR for Th (ESR_{Th}) as:

$$ESR_{Th} = w_s \frac{Th_s}{Th_t} + w_f \frac{Th_f}{Th_t} \tag{10}$$

where Th_s is particulate Th in the slow-sinking small size class, Th_f is particulate Th in the fast-sinking large size class, Th_t is total dissolved and particulate Th and w_s and w_f are the sinking rates of slow and fast particles from van Hulten et al.[54], with values of 2 m d^{-1} and 50 m d^{-1}, respectively. Nickel is assumed to have the same relative affinity for each particle type and size class as Th; however, the absolute scavenging affinity may be different, and the sinking of Ni by reversible scavenging is given as:

$$ESR_{Ni} = R\,ESR_{Th} \tag{11}$$

where R is the relative affinity of Ni for particles compared with ^{230}Th and is tuned during model optimization. Reversible scavenging in the

pattern of ^{231}Pa is done in the same fashion, except using the global distribution of Pa sinking of van Hulten et al.[54].

Reversible scavenging onto particulate Mn oxides is parameterized in the same fashion as scavenging onto POC, except that the concentration of available scavenging sites (S) is based on the distribution of particulate Mn from the global biogeochemical Mn model of van Hulten et al.[55]. Particles are assumed to sink at a rate of 100 m d^{-1}, and the sinking of Ni is determined by a distribution coefficient (K) of adsorbed Ni compared with dissolved Ni.

Finally, a model was tested in which scavenging was assumed to follow the horizontal patterns of surface POC production, but the depth dependence of scavenging was allowed to vary by a power-law distribution (Martin curve) that was different from overall POC remineralization, consistent with work on Th scavenging that shows that POC is less reactive towards Th in the upper water column[28]. We implement this by assuming a global distribution of scavenging sites (S) given by:

$$S = POC_{surf} \left(\frac{z}{z_0} \right)^{-b_S} \tag{12}$$

where POC_{surf} is the surface POC concentration from the P model described in the preceding, z is depth below the compensation depth z_0 (75 m) and b_S is the depth scaling of scavenging sites on POC.

The mean depth of Ni as reported in Fig. 3 and Extended Data Figs. 1–8 and denoted here by z_{Ni} is calculated as:

$$\overline{z_{Ni}} = \frac{\sum v\,[Ni]\,z}{\sum v\,[Ni]} \tag{13}$$

where v, [Ni] and z are the grid-cell volume, Ni concentration and mean grid-cell depth, and the sums extend over all ocean grid cells. Thus, z_{Ni} is simply the mean depth of all Ni atoms in the ocean.

Evaluation of Ni limitation thresholds

Nickel concentrations have been observed to impact a wide variety of biological processes both in culture and in natural communities, many of which have been reviewed in ref. [2]. Some key concentration thresholds at which Ni limitation has a biological impact are depicted in Fig. 4. The exact concentration at which Ni begins to impact physiological processes is not typically ascertained, and thus we note the 'thresholds' at which differences in activity are observed, where the threshold represents a Ni concentration at which a biological process is limited when compared with similar experimental treatments with higher Ni concentrations.

For experiments utilizing natural seawater without added a strong chelator, the threshold is expressed as the total Ni concentration in seawater. For culture experiments, the equilibrium constant for binding of inorganic Ni (Ni') by EDTA is taken as 7.5×10^{10} (ref. [56]), and we assume that half of the Ni in seawater is organically complexed[18], so that the concentration of Ni in seawater (nM) that would yield an equivalent Ni activity (Ni_{sw}) is calculated as:

$$Ni_{sw}(nM) = 2\frac{Ni_{tot}}{7.5\,10^{10}\,EDTA} = 0.0267\frac{Ni_{tot(nM)}}{EDTA(\mu M)} \tag{14}$$

where Ni_{tot} (nM) is the total concentration of Ni in the media and EDTA (μM) is the EDTA concentration (μM).

In the following, we discuss thresholds that are apparently related to the role of Ni in urease, those apparently related to Ni SOD and those associated with [NiFe] hydrogenase. Because the focus of this work is on Ni concentrations in the surface ocean, we do not report data on freshwater organisms. Similarly, we do not report thresholds for methanogenic organisms here, as that process does not occur in the modern open ocean. Both topics are discussed in more detail in ref. [2].

Ni urease

Among marine organisms, corals appear to be especially susceptible to Ni limitation, probably because Ni is a co-factor for the enzyme urease. Coral growth rates (as determined from calcification rate) increased when Ni was added above the ambient concentration of 2 nM for the corals *Acropora muricata* and *Pocillopora damicornis*[57]. A subsequent study indicated that this effect was caused by direct limitation of coral urea uptake because both calcification rates and urea uptake rates increased in these species, as well as in the asymbiotic coral *Dendrophyllia arbuscula*, with Ni added above the 2 nM ambient background concentrations[6].

Because of the role of Ni in the urease enzyme, the response of phytoplankton to Ni additions has been tested where N is supplied in the form of urea ($CO(NH_2)_2$). Dupont et al.[5] tested the co-limitation of natural communities by urea and Ni in a variety of locations and found evidence for higher community growth with 0.75 nM added Ni compared with background concentrations of 4.2 nM Ni in the Costa Rica Upwelling Dome region, although this effect was not observed in several study locations off the coast of California[5]. In laboratory cultures, Oliveira and Antia[58] tested the growth of the diatom *Cyclotella cryptica* in media containing only urea as a nitrogen source and found reduced growth rates at thresholds of 1, 2, 4, 5 and 10 nM Ni compared with higher Ni concentrations. A follow-up study on numerous additional microalgae was performed with natural seawater containing 3.4 nM Ni and various amounts of added Ni[59]; species that were growth limited at 3.4 nM Ni, compared with 8.4 nM Ni, included *Achnanthes brevipes*, *Thalassiosira weissflogii*, *Hymenomonas elongata* and *Prymnesium parvum*. Growth limitation at 8.4 nM, compared with 13.4 nM, was observed for *Rhodomonas* sp., *Achnanthes brevipes*, *Amphidinium carterae*, *Thalassiosira weissflogii*, *Hymenomonas elongata*, *Thalassiosira nordenskioldii* and *Porphyridium cruentum*. Higher concentrations of Ni typically resulted in decreased growth due to toxicity. Similar experiments in EDTA-buffered media showed growth limitation of *Thallassiosira weissflogii* on urea at Ni concentrations of 2 pM and 20 pM, compared with higher Ni concentrations[13]. A study evaluating both Ni growth requirements and Zn uptake in diatoms showed growth-limitation thresholds for the diatom *Thallassiosira pseudonana* (0.004 and 0.02 pM Ni_{sw}) and the diatom *Thallassiosira weissflogii* (0.004, 0.02, 0.2, 0.6, 1.6 and 2 pM Ni).

Ni–urea co-limitation has been less often tested in cyanobacteria compared with eukaryotic algae, but limitation of growth at low Ni in urea-based media has also been demonstrated for two strains of the marine cyanobacterium *Synechococcus*, with strain WH8102 growing more slowly at a 10 pM Ni_{sw} threshold and CC9311 having thresholds at 4, 10 and 30 pM (ref. [25]).

Ni SOD

While culture experiments often show a Ni limitation response when grown with urea, Ni limitation is less common with other nitrogen sources. Yet growth-limitation thresholds were observed for *Synechococcus* WH8102 at 10 pM Ni_{sw} when grown on ammonia and at 4 pM and 15 pM Ni_{sw} when grown on nitrate, attributable to the fact that this strain carries only the Ni form of SOD[25].

Nitrogen-fixing marine cyanobacteria are also reported to be especially susceptible to Ni limitation, an effect that is generally attributed to the importance of Ni SOD to protect against oxidative damage in the presence of abundant sunlight necessary for N fixation. In the presence of abundant Fe and P, *Trichodesmium* growth is limited in natural seawater with 2 nM Ni (ref. [3]). In defined culture media, Ni was found to limit *Trichodesmium* biomass at a threshold of 53 pM, Ni limited SOD activity at thresholds of 13, 27 and 67 pM and a Ni limitation effect on nitrogen fixation rates was observed at thresholds of 13 and 26 pN Ni_{sw}. Subsequent experiments showed that light intensity modulates the thresholds for Ni limitation, with just a single threshold of 13 pM Ni at the lowest light intensity of 100 µE m^{-1} s^{-1}, yet limitations were observed at multiple thresholds of 13, 27 and 67 nM Ni_{sw} at higher light intensities of 670 µE m^{-1} s^{-1} (ref. [160]). This light-dependent Ni requirement can lead to diel changes in N fixation, and the effects of Ni on nitrogen fixation can be dramatic, with 30-fold increases in fixation rates observed above thresholds of 27 pM Ni_{sw} (ref. [35]).

[NiFe] hydrogenase

The nitrogen-fixing cyanobacterium *Cyanothece* is also impacted at low Ni concentrations, with thresholds for H_2 accumulation at 0.04 and 27 pM and a threshold for N_2 fixation at 27 pM Ni_{sw}. However, *Cyanothece* does not apparently possess genes for either Ni SOD or urease, suggesting that this effect may be due to the role of Ni in NiFe uptake hydrogenase[4].

Calculation of β values

Values of β, as shown in Fig. 4 and Supplementary Table 2, were calculated on the basis of individual-cell elemental quotas measured by synchrotron X-ray fluorescence microscopy at a variety of locations, including the Southern Ocean[26], equatorial Pacific[19] and oligotrophic North Atlantic Sargasso Sea[61,62]. In each case, the reported Ni/P cellular quotas are converted to a β according to equation (1) on the basis of local seawater Ni concentrations.

Data availability

Data from the GEOTRACES 2017 IDP are available at https://www.bodc.ac.uk/geotraces/data/idp2017/. Data from the *Tara* Pacific expedition are available at https://doi.org/10.1594/PANGAEA.875582. Data from the US GEOTRACES GP15 transect are available at https://github.com/MTEL-USC/nickel-model.

Code availability

Model code for this work is available at https://github.com/MTEL-USC/nickel-model and can be run within the AWESOME OCIM modelling environment available at https://github.com/profseth/awesomeOCIM.

References

40. Donat, J. R., Lao, K. A. & Bruland, K. W. Speciation of dissolved copper and nickel in South San Francisco Bay: a multi-method approach. *Anal. Chim. Acta* **284**, 547–571 (1994).

41. Hawco, N. J. et al. Metal isotope signatures from lava–seawater interaction during the 2018 eruption of Kīlauea. *Geochim. Cosmochim. Acta* **282**, 340–356 (2020).

42. Saad, E. M. et al. Effect of cleaning methods on the dissolution of diatom frustules. *Mar. Chem.* **224**, 103826 (2020).

43. Andersen, M. B. et al. The Zn abundance and isotopic composition of diatom frustules, a proxy for Zn availability in ocean surface seawater. *Earth Planet. Sci. Lett.* **301**, 137–145 (2011).

44. Ellwood, M. J. & Hunter, K. A. The incorporation of zinc and iron into the frustule of the marine diatom *Thalassiosira pseudonana*. *Limnol. Oceanogr.* **45**, 1517–1524 (2000).

45. Sunda, W. G., Price, N. M. & Morel, F. M. M. Trace metal ion buffers and their use in culture studies. *Algal Cult. Tech.* **4**, 35–63 (2005).

46. Tovar-Sanchez, A. et al. A trace metal clean reagent to remove surface-bound iron from marine phytoplankton. *Mar. Chem.* **82**, 91–99 (2003).

47. Capone, D. G. & Hutchins, D. A. Microbial biogeochemistry of coastal upwelling regimes in a changing ocean. *Nat. Geosci.* **6**, 711–717 (2013).

48. Cutter, G. et al. *Sampling and Sample-Handling Protocols for GEOTRACES Cruises* (GEOTRACES International Project Office, 2017); https://doi.org/10.25607/OBP-2

49. Schlitzer, R. et al. The GEOTRACES Intermediate Data Product 2017. *Chem. Geol.* **493**, 210–223 (2018).

50. Gorsky, G. et al. Expanding *Tara* oceans protocols for underway, ecosystemic sampling of the ocean–atmosphere interface during *Tara* Pacific expedition (2016–2018). *Front. Mar. Sci.* **6**, 750 (2019).

51. Jensen, L. T., Wyatt, N. J., Landing, W. M. & Fitzsimmons, J. N. Assessment of the stability, sorption, and exchangeability of marine dissolved and colloidal metals. *Mar. Chem.* **220**, 103754 (2020).

52. DeVries, T. The oceanic anthropogenic CO_2 sink: storage, air–sea fluxes, and transports over the industrial era. *Glob. Biogeochem. Cycles* **28**, 631–647 (2014).

53. Holzer, M., Primeau, F. W., DeVries, T. & Matear, R. The Southern Ocean silicon trap: data-constrained estimates of regenerated silicic acid, trapping efficiencies, and global transport paths. *J. Geophys. Res. Oceans* **119**, 313–331 (2014).

54. van Hulten, M., Dutay, J.-C. & Roy-Barman, M. A global scavenging and circulation ocean model of thorium-230 and protactinium-231 with improved particle dynamics (NEMO–ProThorP-0.1). *Geosci. Model Dev.* **11**, 3537–3556 (2018).

55. van Hulten, M. et al. Manganese in the west Atlantic Ocean in the context of the first global ocean circulation model of manganese. *Biogeosciences* **14**, 1123–1152 (2017).

56. Westall, J. C. et al. *MINEQL: A Computer Program for the Calculation of Chemical Equilibrium Composition of Aqueous Systems* (Water Quality Laboratory, Ralph M. Parsons Laboratory for Water Resources and Environmental Engineering, and Department of Civil Engineering, Massachusetts Institute of Technology, 1976).

57. Biscéré, T. et al. Nickel and ocean warming affect scleractinian coral growth. *Mar. Pollut. Bull.* **120**, 250–258 (2017).

58. Oliveira, L. & Antia, N. J. Evidence of nickel ion requirement for autotrophic growth of a marine diatom with urea serving as nitrogen source. *Br. Phycol. J.* **19**, 125–134 (1984).

59. Oliveira, L. & Antia, N. J. Nickel ion requirements for autotrophic growth of several marine microalgae with urea serving as nitrogen source. *Can. J. Fish. Aquat. Sci.* **43**, 2427–2433 (1986).

60. Ho, T.-Y., Chu, T.-H. & Hu, C.-L. Interrelated influence of light and Ni on *Trichodesmium* growth. *Front. Microbiol.* **4**, 139 (2013).

61. Nuester, J., Vogt, S., Newville, M., Kustka, A. & Twining, B. The unique biogeochemical signature of the marine diazotroph *Trichodesmium*. *Front. Microbiol.* **3**, 150 (2012).

62. Twining, B. S., Nuñez-Milland, D., Vogt, S., Johnson, R. S. & Sedwick, P. N. Variations in *Synechococcus* cell quotas of phosphorus, sulfur, manganese, iron, nickel, and zinc within mesoscale eddies in the Sargasso Sea. *Limnol. Oceanogr.* **55**, 492–506 (2010).

Author contributions

Phytoplankton culturing and analysis of culture samples was done by R.L.K., X.B., S.-C.Y., E.A.S., F.F., M.I.S. and D.A.H. Analyses of natural materials and seawater samples were completed by S.-C.Y., X.B., N.T.L., J.N.F. and T.M.C. Chemical experiments and analysis were performed by S.G.J. Modelling was undertaken by S.G.J. with the assistance of H.L., B.P., M.H. and L.W. The manuscript was written by S.G.J. with advice and input from all co-authors.

Competing interests

The authors declare no competing interests.

Additional information
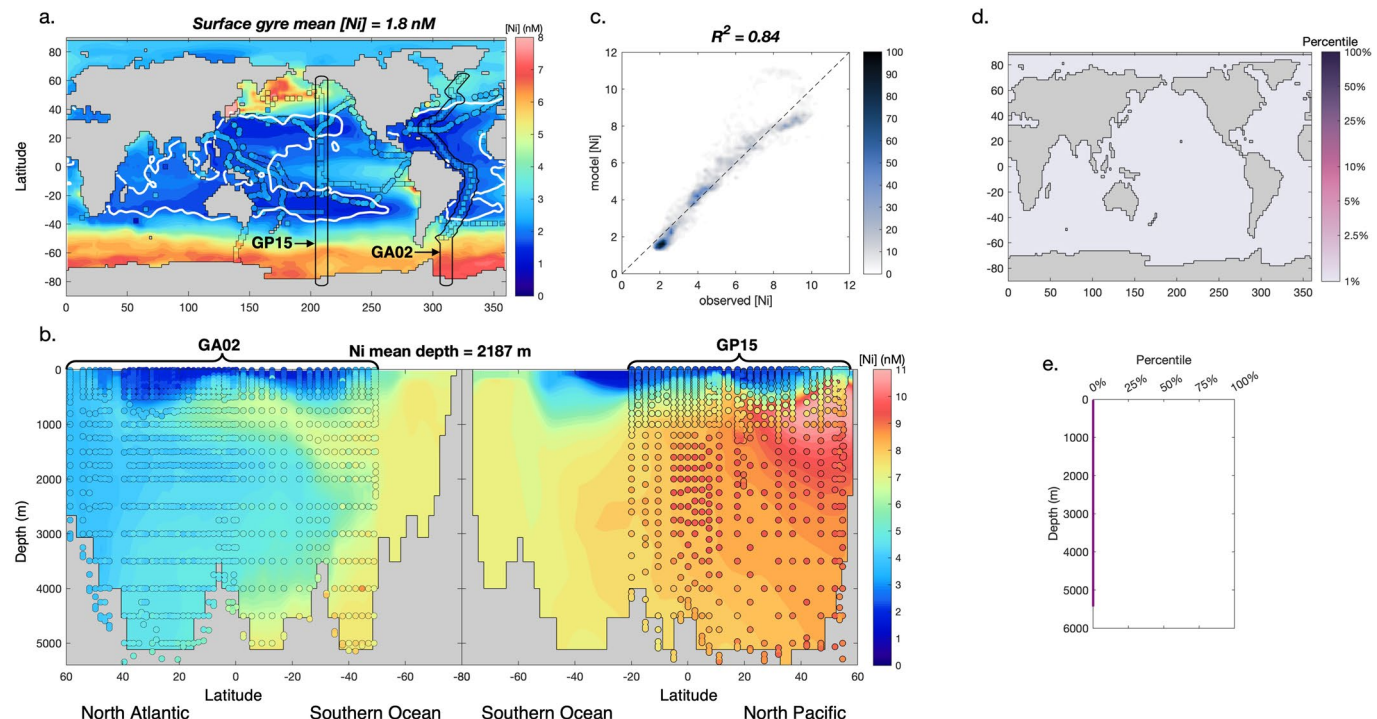
Extended data is available for this paper at https://doi.org/10.1038/s41561-022-01045-7.

Supplementary information The online version contains supplementary material available at https://doi.org/10.1038/s41561-022-01045-7.

Correspondence and requests for materials should be addressed to Seth G. John.
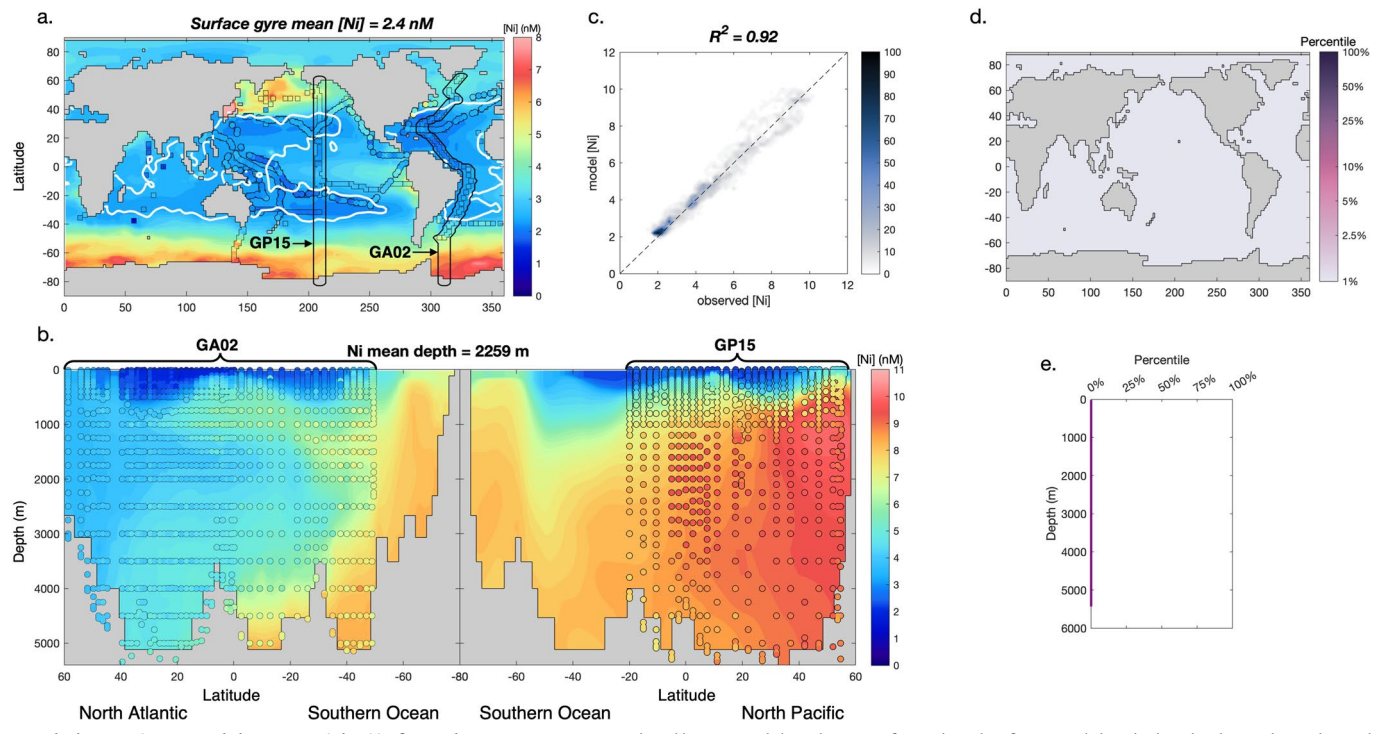
Peer review information *Nature Geoscience* thanks Benjamin Twining and the other, anonymous, reviewer(s) for their contribution to the peer review of this work. Primary Handling Editor: Rebecca Neely, in collaboration with the *Nature Geoscience* team.

Reprints and permissions information is available at www.nature.com/reprints.
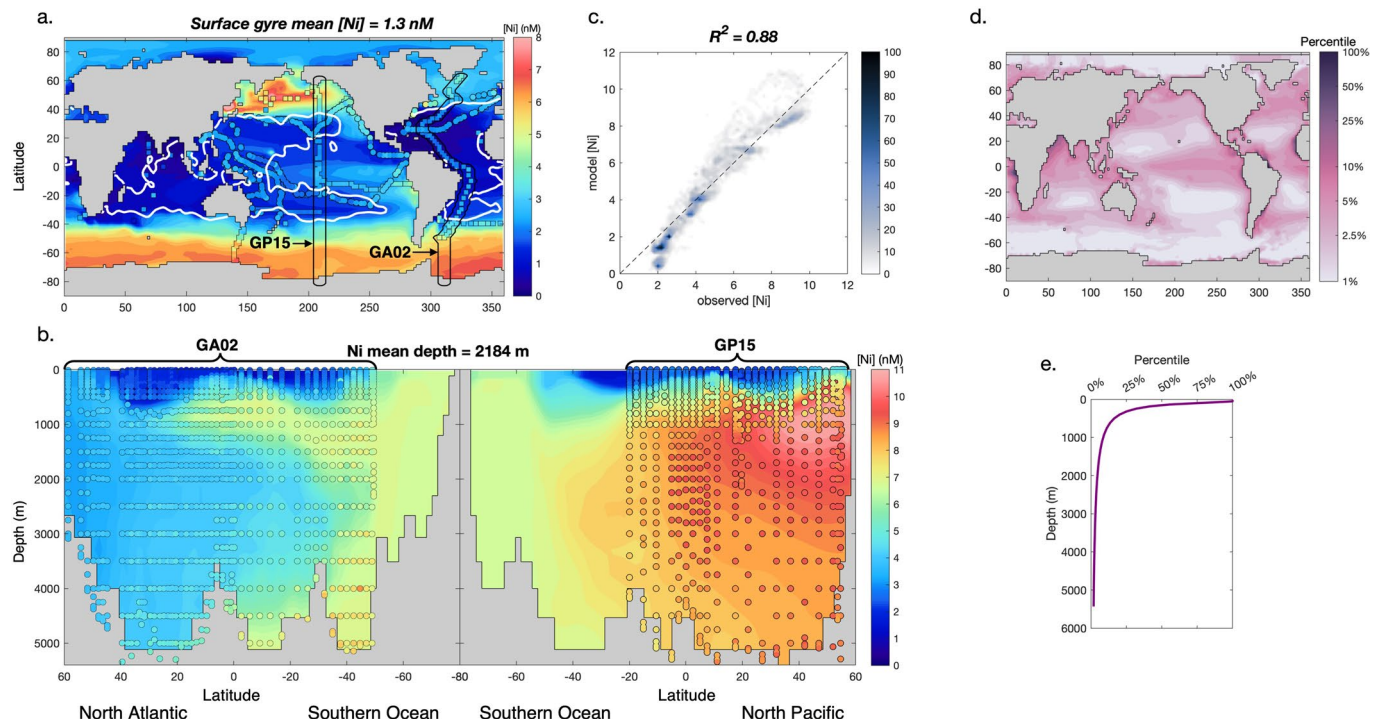
Extended Data Fig. 1 | Base model output. Patterns in vertical and horizontal distribution of simulated Ni for a model including only biological uptake and remineralization of Ni in soft-tissue. **a**) Comparison between observations (colored circles) and optimized model output (background color) are shown for the surface ocean, with white lines delineating the boundaries of the oligotrophic gyre at 0.2 μM PO_4^{2-}, and black lines showing the location of depth transect data. **b**) Comparison between observations and optimized model output are shown for depth transects in the Atlantic and Pacific Ocean, which include GEOTRACES transects GA02 and GP15, respectively. The Ni mean depth reported above this panel refers to the average depth of model-predicted Ni in the global ocean, which can be compared to mean depths of 2174 m and 2533 m for P and Si,
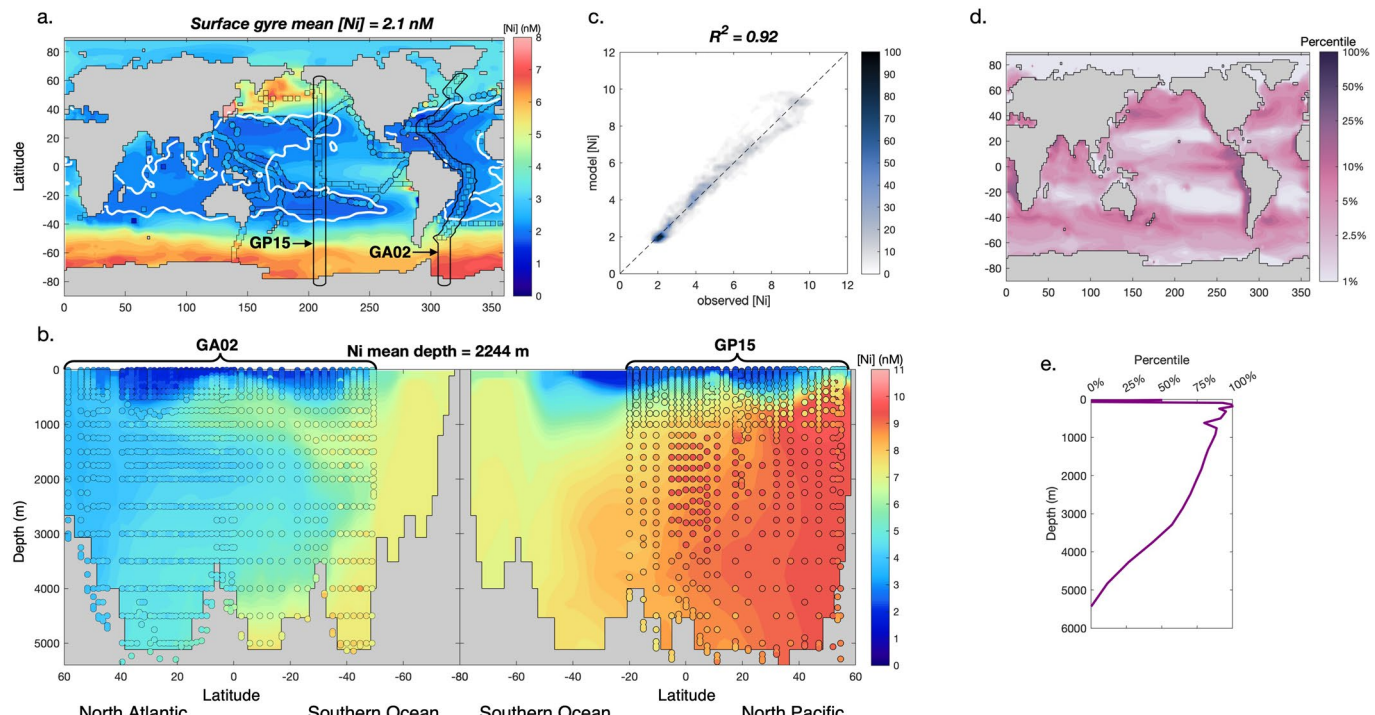
respectively, based on World Ocean Atlas 2009 data. **c**) The global fit between model and observed Ni, with the colorscale reflecting the relative data density as a percentage compared to maximum data density. **d**) Horizontal patterns in global depth integrated scavenging flux of Ni (which has no value for this model because no scavenging process was included), presented as a percentage of the maximum scavenging intensity. **e**) vertical patterns in horizontally integrated Ni scavenging flux (which has no value for this model because no scavenging process was included), presented as a percentage of the maximum scavenging intensity. Additional information about optimized model parameters and model performance metrics are presented in Table ED1.
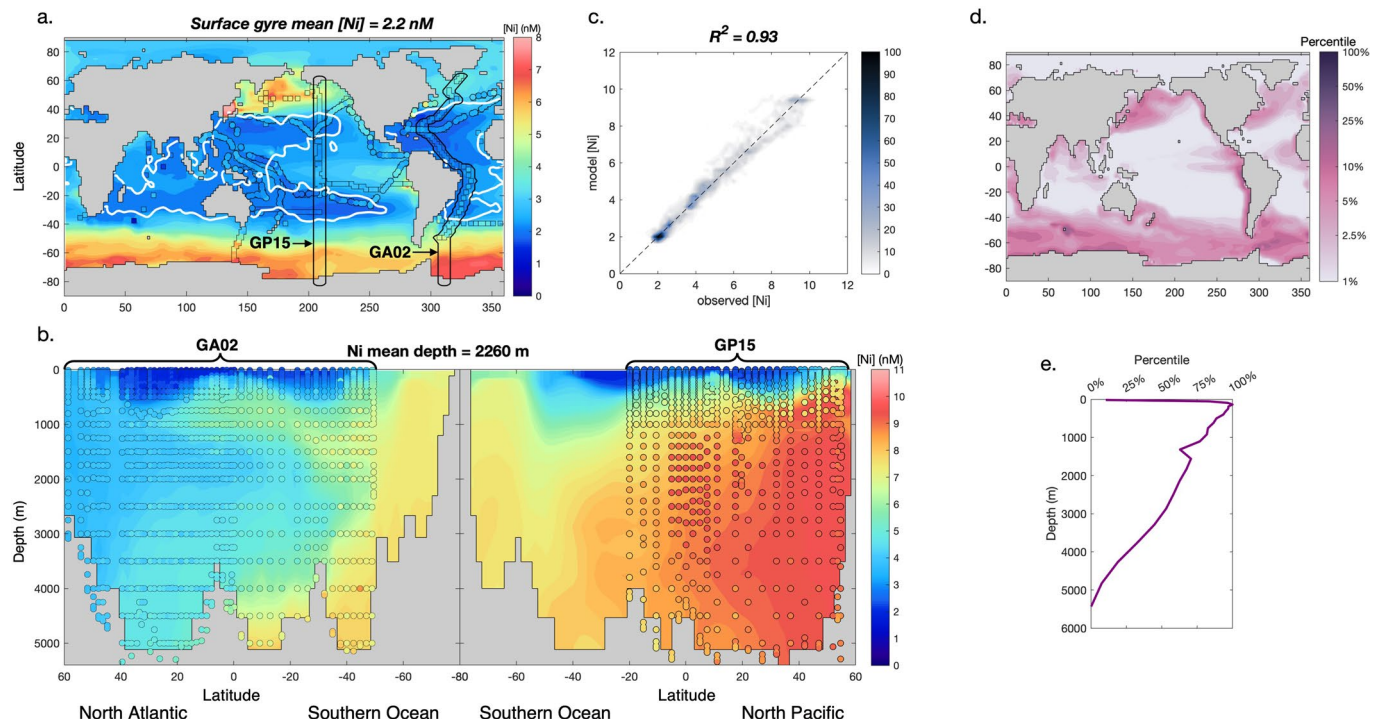
Extended Data Fig. 2 | Model output with Ni in frustules. Patterns in vertical and horizontal distribution of simulated Ni for a model including biological uptake and remineralization of Ni in soft-tissue, and the biological uptake and remineralization of Ni due to incorporation in diatom silicate frustules. Panels are the same as for Extended Data Fig. 1.
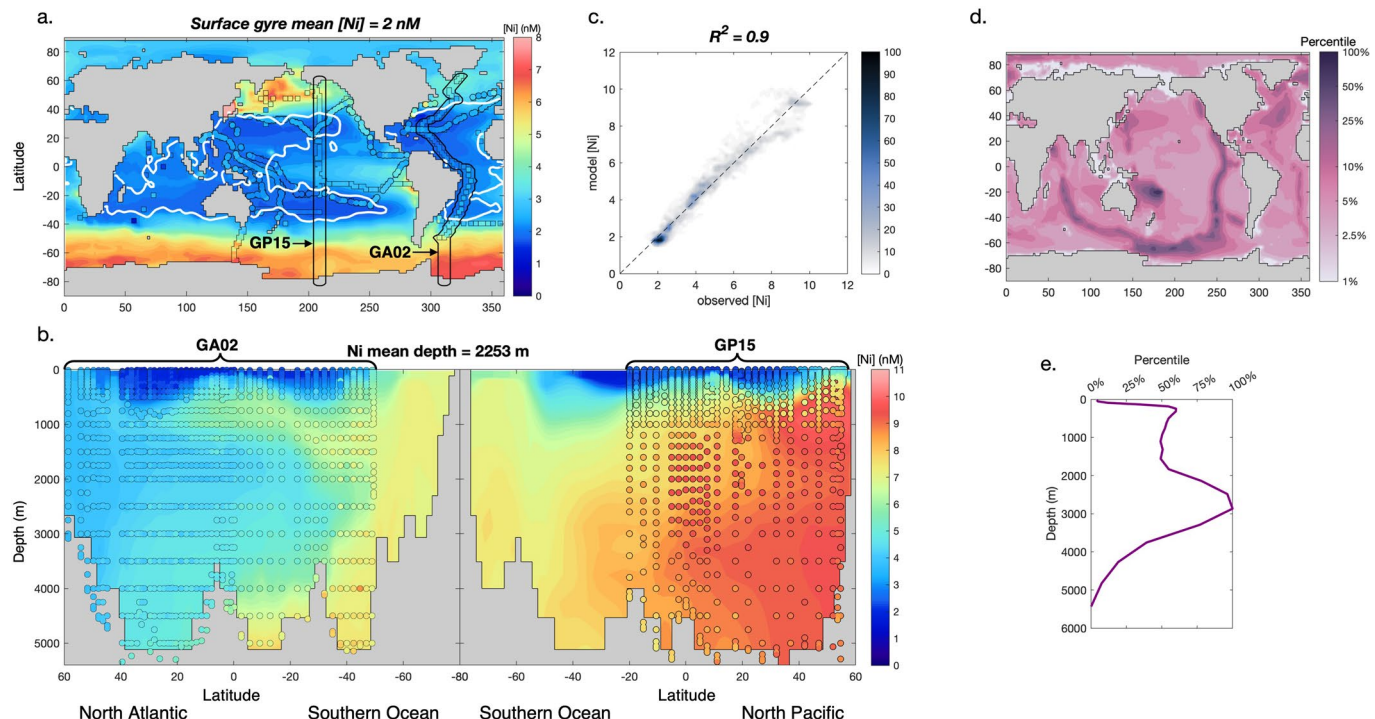
Extended Data Fig. 3 | Model output with reversible scavenging onto POC. Patterns in vertical and horizontal distribution of simulated Ni can be evaluated for models with various parameterizations of reversible scavenging, here showing a model with reversible scavenging onto POC as determined in Weber et al.[12]. Panels are the same as for Extended Data Fig. 1.
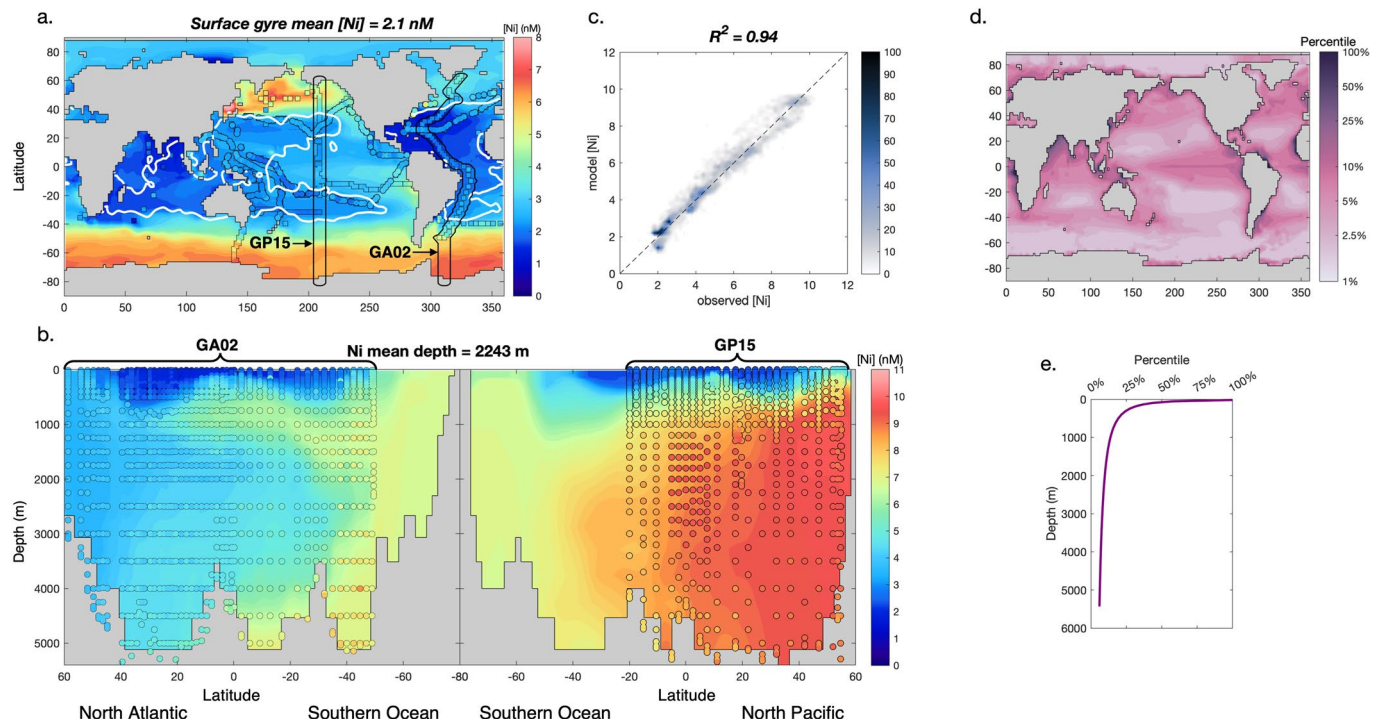
Extended Data Fig. 4 | Model output with reversible scavenging like Th. Patterns in vertical and horizontal distribution of simulated Ni can be evaluated for models with various parameterizations of reversible scavenging, here showing a model with reversible scavenging taking the same patterns as Th scavenging from Hulten et al.[54]. Panels are the same as for Extended Data Fig. 1.

Extended Data Fig. 5 | Model output with reversible scavenging like Pa. Patterns in vertical and horizontal distribution of simulated Ni can be evaluated for models with various parameterizations of reversible scavenging, here showing a model with reversible scavenging taking the same patterns as Pa scavenging from Hulten et al.[54]. Panels are the same as for Extended Data Fig. 1.
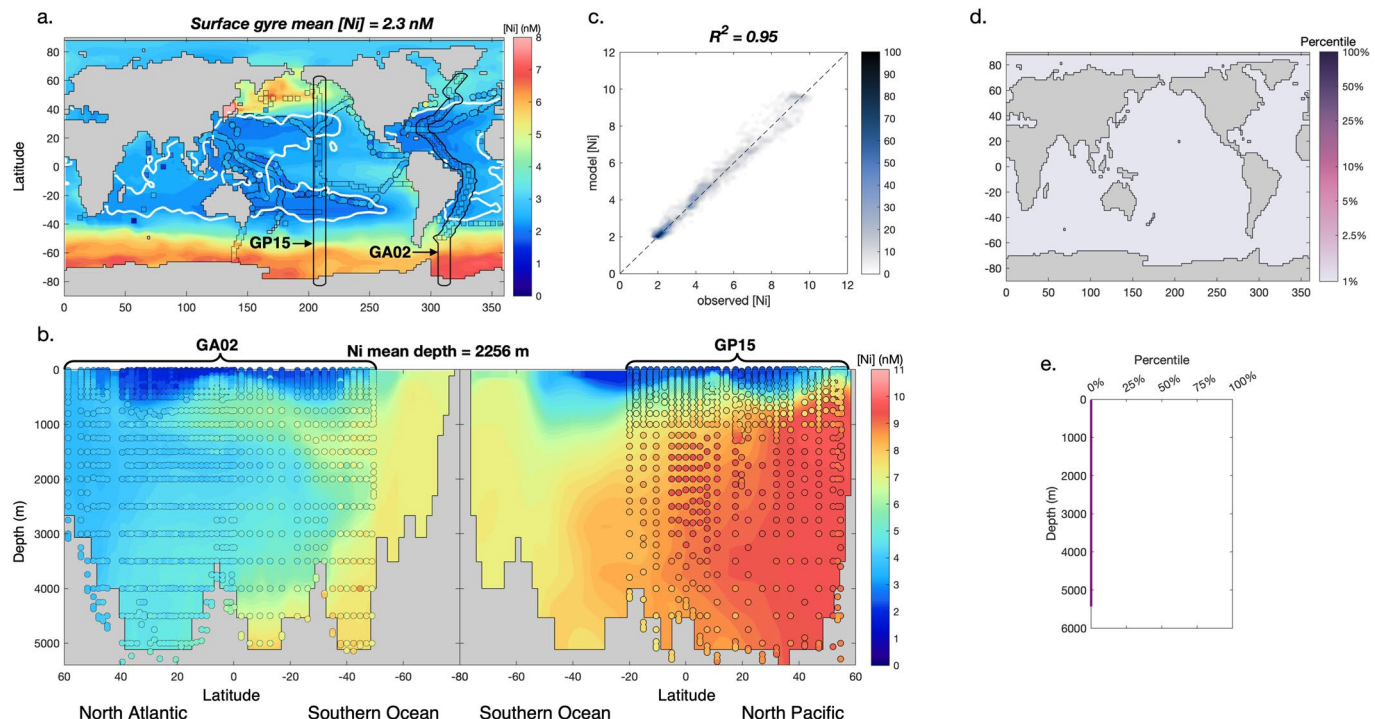
Extended Data Fig. 6 | Model output with reversible scavenging onto Mn oxides. Patterns in vertical and horizontal distribution of simulated Ni can be evaluated for models with various parameterizations of reversible scavenging, here showing a model with reversible scavenging onto particulate Mn oxides, based on a Mn model from van Hulten et al.[55]. Panels are the same as for Extended Data Fig. 1.
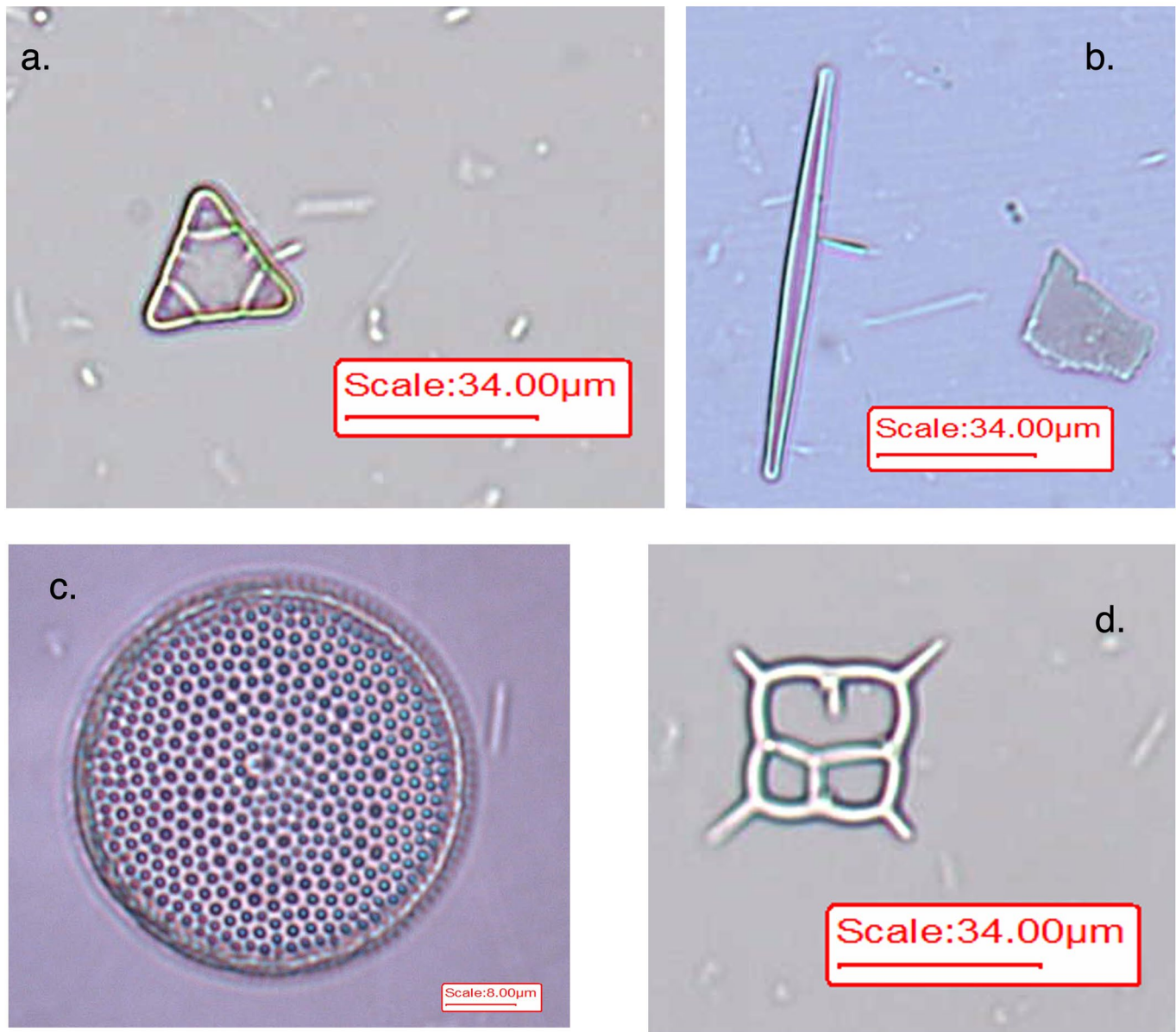
Extended Data Fig. 7 | Model output with reversible scavenging onto POC, variable *b*. Patterns in vertical and horizontal distribution of simulated Ni can be evaluated for models with various parameterizations of reversible scavenging, here showing a model with reversible scavenging onto POC based on Weber et al.[12], with the vertical distributions of scavenging sites on POC determined from an optimized power-law equation. Panels are the same as for Extended Data Fig. 1.

Extended Data Fig. 8 | Model output with deeper organic Ni remineralization. Patterns in vertical and horizontal distribution of simulated Ni, here showing a model where Ni is allowed to remineralize according to a 'Martin curve' power law, except that the b exponent is optimizable for Ni instead of being tied to the remineralization of P. Panels are the same as for Extended Data Fig. 1.

Extended Data Fig. 9 | Diatoms collected from the North Pacific. Light microscopy micrographs showing persistence of intact and undamaged biogenic silica shells after removal of cellular organic material using HNO_3. Shown are HNO_3 cleaned silica frustules of **a**) the centric diatom *Triceratium* (100X magnification), **b**) the pennate diatom *Pseudo-nitzschia* (100X magnification), and **c**) the centric diatom *Coscinodiscus* (400X magnification). Even delicate shells of **d**) the silicoflagellate *Dictyocha* (100X magnification) came through the HNO_3 digestion procedure intact, as did similarly fragile silica shells of radiolarians (not shown). All cells shown were collected on a 53 µm filter.